Available online at www.sciencedirect.com
ScienceDirect
Geochimica et Cosmochimica Acta 73 (2009) 6918–6936
Geochimica et Cosmochimica Acta
www.elsevier.com/locate/gca

Structure, thermodynamic and transport properties of $CaAl_2Si_2O_8$ liquid. Part I: Molecular dynamics simulations

Frank J. Spera [a,*], Dean Nevins [a], Mark Ghiorso [b], Ian Cutler [a]

[a] Department of Earth Science, University of California-Santa Barbara, Santa Barbara, CA 93106, USA
[b] OFM-Research, 7336 24th Ave. NE Seattle, WA 98115, USA

Received 25 February 2009; accepted in revised form 13 August 2009; available online 23 August 2009

Abstract

Molecular dynamics simulations for liquid $CaAl_2Si_2O_8$ have been carried out at 72 state points spanning ranges in density (ρ: 2398–4327 kg/m^3), temperature (T: 3490–6100 K) and pressure (P: 0.84–120 GPa) relevant to geosystems. The atomic scale structure of the melt is determined by analysis of nearest neighbor coordination statistics as a function of T and P. Dramatic structural change occurs as pressure increases especially for $0 < P < 20$ GPa at all temperatures. Changes in structure are encapsulated by examining the coordination of Si, Al, Ca and O around oxygen and *vice versa*. Si and Al change from predominantly fourfold at low-P to dominantly sixfold for $P > \sim 20$ GPa. Pentahedrally coordinated Si and Al in distorted trigonal bipyramids attain abundance maxima corresponding to ~60% of total (Si, Al)O_n at 3–5 GPa and weakly depend on T. The coordination of Ca by oxygen increases from 7 to 10 for $0 < P < 20$ GPa and changes slowly for $P > 20$ GPa at 3500 K. Similar behavior is seen at 6000 K except that the interval of rapid changes occurs at higher pressure. Oxygen with only one nearest Si or Al neighbor (i.e., non-bridging oxygen, NBO) decreases whereas oxygen with two or three nearest neighbors of Si, Al or Ca increases as pressure increases. Changes in melt structure are reflected in the variation of thermodynamic and transport properties of the liquid. Values of the self-diffusivities of Ca, Al, Si and O are fit to a modified Arrhenian expression and compare well to limited laboratory data. Self-diffusivities are best fit using 'low P' and 'high-P' expressions, identical in form but with different parameters, with activation energies and activation volumes in the range 150–200 kJ/mol and +5 to −1 cm^3/mol, respectively. Green–Kubo calculations for liquid shear viscosity are presented and compare well with limited laboratory results. Application of the Eyring model to determine the characteristic size and number of atoms in the activated cluster based on independently computed D and η suggests that the activated cluster decreases from ~8 to ~3 atoms from low to high pressure while its characteristic size shrinks from ~14 Å to ~3 Å providing insight into dynamics of atom mobility and possible cooperative behavior. The equation of state and variation of internal energy with T and V are used in Part II (Ghiorso et al., 2009) to derive a comprehensive thermodynamic description of liquid $CaAl_2Si_2O_8$. This is best accomplished by allowing for EOS expressions broken into high and low pressure intervals consistent with coordination statistics and MD-derived transport properties.

1. INTRODUCTION

This paper is part of a series in which the structure, thermodynamic and transport properties of molten multicomponent silicates relevant to geochemical and geodynamical problems are investigated at elevated temperatures (2500–5000 K) and pressures (0–135 GPa) by combining Molecular Dynamics (MD) simulations with macroscopic equation of state (EOS) and transport property analysis. So far relatively unpolymerized melts such as Mg_2SiO_4 and $MgSiO_3$ have been studied in some detail in order to construct of equations of state and transport property relations (e.g., Stixrude and Karki, 2005; Wan et al., 2007; de Koker et al., 2008; Martin et al., 2009; Nevins et al., 2009).

* Corresponding author. Tel.: +1 805 893 4880.
E-mail address: spera@geol.ucsb.edu (F.J. Spera).

0016-7037/$ - see front matter © 2009 Elsevier Ltd. All rights reserved.
doi:10.1016/j.gca.2009.08.011

Although several natural or archetypical silicate liquids have been investigated by laboratory (e.g., shock wave, see Akins et al., 2004) or computational methods (e.g., Guillot and Sator, 2007a,b; Lacks et al., 2007), a multicomponent silicate liquid thermodynamic and transport property model valid throughout the Earth's mantle remains elusive. Although the conceptual basis for a fully multicomponent thermodynamic treatment is on hand (e.g., see Ghiorso 2004a,b; Ghiorso and Kress, 2004) the lack of EOS information at elevated temperature and pressure for multicomponent liquids has hampered development of models useful for geochemical and geophysical applications. Construction of an EOS requires approximately 75–100 state points more or less evenly distributed over the appropriate P–T region; a few P–T points on a few compositions are woefully insufficient. In this study (Part I) and its companion (Part II, Ghiorso et al., 2009) molten $CaAl_2Si_2O_8$ is studied in detail. In Part I (this study) details on the MD simulations, retrieved thermodynamic and transport properties and melt structures are provided and compared with available laboratory information. These results are used in Part II (Ghiorso et al., 2009) to construct a thermodynamic equation of state for liquid $CaAl_2Si_2O_8$ and to compare the EOS predictions with shock wave (Asimow and Ahrens, 2008) and other laboratory thermodynamic data.

Knowledge of the properties of naturally occurring silicate liquids is key for understanding the current and previous dynamical states of the Earth. For example, quantitative information regarding liquid shear viscosity, the self-diffusivity of oxygen, silicon, aluminum, the alkalis, alkaline earths and transition metals and the thermal and ionic conductivity of molten silicates is indispensable for analysis of magma transport phenomena. The thermodynamic properties and structure of molten silicates are also relevant to magma genesis and crystal-liquid equilibria including the thermal properties and trace element systematics of erupted liquids. A number of arguments suggest that the Earth and other terrestrial planets underwent substantial or complete melting during formation by collisional accretion (e.g., Ohtani et al., 1985; Abe, 1997; Debaille et al., 2008). In the case of Earth, subsequent giant Moon-forming impact also deposited large amounts of heat (Canup and Agnor, 2000; Solomatov, 2000; Canup, 2004). The state of the mantle following magma ocean solidification set the initial conditions for growth and evolution of the lithosphere, hydrosphere and the atmosphere and mediated the start of plate tectonics on Earth (Anderson, 2007). On the Moon, the formation of a plagioclase-rich crust by floatation upon the lunar magma ocean was of paramount importance. Many terrestrial (silicate plus metal) exoplanets circling nearby (<1000 lightyear distant) stars await discovery (Valencia et al., 2007) and so the necessity of understanding the properties of molten silicates at extreme conditions on 'super earths' will undoubtedly arise in the future. Arguments have been made for the presence of localized regions of melt along the core–mantle boundary of the Earth today (Garnero et al., 1993; Revenaugh and Sipkin, 1994; Williams and Garnero, 1996; Revenaugh and Meyer, 1997). These few illustrative examples underscore the importance of understanding the properties of multicomponent silicate liquids for application to myriad geochemical and geodynamical problems on Earth and other planets.

In addition to geochemical and geodynamical applications, an understanding of the amorphous state (liquids and glasses), specifically the relationship between liquid structure, the EOS and transport properties, is of interest in its own right. Liquid–liquid phase separation, in which two liquids of distinct composition coexist at a single state point, are quite common in natural systems and have long been studied (e.g., Roedder, 1951; Philpotts, 1976). There is now growing interest in a more unusual behavior. This phenomenon, whereby a one-component system can exist as two liquid or amorphous phases having an identical chemical composition but distinct density and structure, is termed polyamorphism (Grimsditch, 1984). Phase transitions between such distinctly structured liquids occur without change in composition but instead with a change in density (Tanaka, 2000). Experimental evidence for polyamorphism has been found in molten silica, H_2O, and binary melts in the system Al_2O_3–Y_2O_3 among other compositions (e.g., Aasland and McMillan, 1994; Debenedetti 1996; Senker and Rossler, 2001; Brazhkin and Lyapin, 2003; Skibinsky et al., 2004). Polyamorphism for a given composition can be predicted from thermodynamic analysis provided a robust EOS is available. Due to advances in both hardware and software within the last decade a sufficient number (~70) of state points for a single composition can now be routinely investigated by MD simulation thereby enabling accurate construction of an EOS consistent with a given effective pair potential.

The liquid state arises from a delicate balance between the 'packing' of atoms (related to the configurational entropy) and the 'cohesive' forces between atoms (related to the internal energy). The details of this balance determine liquid structure, its dependence on temperature and density (pressure) and material properties-both thermodynamic and transport (Barrat and Hansen, 2003). Two specific aspects are particularly noteworthy. The first is the work of Rosenfeld and Tarazona (1998) who have developed free energy functionals for systems characterized by continuous ('soft') potentials such as those used to study silicate geoliquids. Their model posits that the fluid Madelung (potential) energy scales with T according to $T^{3/5}$. Rosenfeld–Tarzona (RT) scaling can be tested using MD results and has been found quite robust and hence extremely useful in EOS construction from MD simulations (Ghiorso et al., 2008) because it provides a rationale for interpolation and extrapolation. A second point, now widely appreciated, is that pressure has a dramatic effect on melt structure (e.g., Nevins and Spera, 1998; Bryce et al., 1999; Lacks et al., 2007; Guillot and Sator, 2007b). An advantage of the MD method is that complete coordination number statistics are available at each state point, essential information for constraining mixing models. The combination of coordination statistics with RT scaling provides a framework for a multicomponent model of the thermodynamics of molten silicates. For multicomponent systems, entropic effects associated with the mixing of various coordination polyhedra are crucial to the development of accurate

macroscopic models (e.g., Ghiorso, 2004a). Although accurate laboratory measurements are the gold standard for EOS development, the wide range of coverage in composition, temperature and pressure needed for application to planet interiors means that computational methods will play an important role in the future.

In this study (Part I), we report the details of MD simulations for molten $CaAl_2Si_2O_8$. Simulations have been carried out at 72 state points for density (ρ), T and P ranges of 2398–4327 kg/m^3, 3490–6100 K and 0.84–120 GPa, respectively. The raw data are presented in tabular form and the self-diffusivity (D_i) of Ca, Al, Si and O and shear viscosity (η) variation with P and T are presented. In Part II, a detailed macroscopic EOS analysis is derived based on the MD results and additional theoretical insights. We begin by presenting the general form of the simple pair-wise-additive potential used in these studies. This is followed by a description of the molecular dynamics (MD) method and details of the calculations applied to molten $CaAl_2Si_2O_8$. Thermodynamic properties including the thermal pressure, isobaric expansivity (α), isothermal compressibility (β), isochoric heat capacity (C_V) and Grüneisen's parameter (γ) are presented at each state point in tabular form (electronic annex EA-1 and EA-2). We show how RT scaling can be used to obtain comprehensive expressions for the internal energy as a function of volume and temperature, $E(V, T)$ which are used in Part II to build the EOS. A nearest neighbor analysis as a function of pressure (or volume) along selected isotherms is given. Comprehensive tables for coordination statistics are given in electronic annex EA-3. Values of the self-diffusivities of Ca, Al, Si and O are presented spanning the range of P and T of the MD simulations and the close connection between self-diffusion and melt structure at the scale of 0.2–0.5 nm is elucidated. Green–Kubo calculations for the shear viscosity of molten $CaAl_2Si_2O_8$ at elevated temperature and pressure are presented enabling a test of the phenomenological Stokes–Einstein and Eyring models for predicting viscosity from self-diffusion data and providing insight into the size of the activated complex involved in diffusion and viscous flow.

2. PREVIOUS WORK AND PROSPECTUS

Previous studies of liquid $CaAl_2Si_2O_8$ by MD simulations have been carried out by Scamehorn and Angell (1991), Nevins and Spera (1998) and Morgan and Spera (2001a,b). A highlight from the Nevins and Spera (1998) study was an explanation of laboratory data for the solubility of noble gas Ar as a function of pressure (e.g., see Chamorro-Perez et al., 1998) in molten $CaAl_2Si_2O_8$. Analysis of the coordination statistics from the MD simulations showed that the decreasing abundance of $(Si,Al=T)O_4$ and TO_5 polyhedra and concomitant increase in edge-sharing TO_6 octahedra with increasing pressure destroys the high compressibility open ring structure of the melt. Recall that in crystals of anorthite at low pressure, TO_4 tetrahedra corner share to form 8-membered rings that define a large inter-ring site. The destruction of the TO_4 and TO_5 corner-sharing network drastically decreases the number of available ring sites where Argon and other noble gases can be accommodated in accord with laboratory solubility data. Recent additional experimental solubility studies (Bouhifd et al., 2008) confirm this view. Morgan and Spera (2001a,b) focused primarily on the thermodynamics and dynamics of the computer glass transition and did not specifically explore the effects of pressure. Ghiorso (2004b) used the results from Nevins and Spera (1998) and Morgan and Spera (2001a,b) to develop a provisional equation of state of liquid $CaAl_2Si_2O_8$ spanning the density range 2400–3800 kg/m^3 at 4000 K. This work is vastly expanded upon in this study.

Due to dramatic improvements in algorithms and computing resources, it is now possible to obtain extensive coverage in P–T–V coordinates for multicomponent silicate liquids that span the range of temperature and pressure relevant to the Earth's mantle. Simulations with 10^4 (or more) particles for periods up to 5 nanoseconds (ns) can be routinely performed. This is important for the accurate construction of the EOS and determination of transport properties. MD simulations of the type performed here generate microcanonical (NEV) ensemble-averaged properties at PT state points defined by mean simulation values with associated fluctuations that arise due to the finite number of particles (N) in the simulated system. The fluctuations in temperature (σ_T) and pressure (σ_p) scale as $N^{-1/2}$ where N is the number of atoms in the simulation (McQuarrie, 1976). Hence there is an inherent uncertainty in any ensemble-averaged property (e.g., diffusivity, isochoric heat capacity, internal energy, shear viscosity, etc.) associated with intrinsic fluctuations in state point values (i.e., temperature and pressure in the NEV ensemble). The $N^{-1/2}$ scaling implies that the uncertainty in temperature or pressure is four times smaller in a MD simulation of, say, $N = 8000$ atoms compared to one of $N = 500$ atoms, for example. Large particle number simulations are required to accurately compute material properties for a given potential (e.g., see Rustad et al., 1990; Kawamura, 1991) in order to reduce uncertainties in temperature and pressure associated with a given property. For transport properties (e.g., shear viscosity, phonon thermal conductivity, ionic conductivity) defined by integral time-correlation functions from Green–Kubo theory (Kubo, 1966), long simulations, typically 2–10 nanoseconds (ns), are necessary to reduce uncertainties (Nevins and Spera, 2007). Long simulation times on large systems have only become practical recently. We exploit this capability in this and related works.

3. METHODS

3.1. *Ab initio* versus effective pair potential models

In principle, knowledge about a material is obtained from the quantum mechanical wave function. This is obtained by solving the Schrödinger equation for the many electron system. In practice solving such an N-body problem is not possible. Density Functional Theory (DFT) developed by Kohn and Sham (1965) based on the theory of Hohenberg and Kohn (1964) can be used to approximate the energy. The fundamental parameter in DFT is the electron charge density rather than electron wave functions.

The *N*-electron problem is expressed as *N* one-electron equations where each electron interacts with all other electrons via an effective exchange–correlation potential. These interactions are calculated using the local density approximation to exchange and correlation. Plane wave basis sets and total energy pseudopotential techniques are used to solve the Kohn–Sham one electron expressions. The Hellmann–Feynman theorem is then used to compute the forces required to integrate the equations of motion as required in molecular dynamics simulations (Car and Parrinello, 1985). This method of 'First-Principles' or *ab initio* Molecular Dynamics (FPMD) has been applied to small systems, typically of $N \sim 100$ particles for molten SiO_2, SiO_2–H_2O, Mg_2SiO_4, $MgSiO_3$ and $MgSiO_3$–H_2O (Horbach and Kob, 2002; Pohlmann et al., 2004; Stixrude and Karki, 2005; Wan et al., 2007; de Koker et al., 2008; Mookherjee et al., 2008). With further approximations, larger systems up to ~1000 atoms can be studied (Ordejon et al., 1996; Soler et al., 2002) although these methods has not yet been applied to geochemical systems. Insights into the current limitations of DFT and the role of intermolecular potentials are discussed by Stone (2008) and Cohen et al. (2008).

A simpler approach based on effective pair potentials is adopted in this series of studies in part to enable study of relatively large systems ($N \sim 10^4$) for the long durations (~2 ns) necessary for determination of transport properties (Nevins and Spera, 2007) and robust equations of state. Large *N*-long duration simulations are not yet routinely feasible using *ab initio* methods. Although Effective Pair-potential Molecular Dynamics (EPPMD) is less 'exact' than FPMD, when comparisons are made between FPMD and EPPMD results are often quite reasonable, although difference do remain, provided effective pair potentials (Filippini and Gavezzotti, 1993) are carefully developed (e.g., Cao et al., 1994; Oganov et al., 2001; Saika-Voivod et al., 2001, 2004; Stixrude and Karki, 2005; Lacks et al., 2007; Wan et al., 2007; Martin et al., 2009; Nevins et al., 2009). An additional example is the favorable comparison between EPPMD and FPMD results (Karki et al., 2006; Lacks et al., 2007, respectively) for the molar volume of MgO liquid at 3000 K and zero pressure: 16.3 cm^3/mol versus 16.5 cm^3/mol, respectively. Collectively, these comparisons suggest that well-constructed effective pair potentials can provide a reliable means for studying the structure, thermodynamics and transport properties of silicate liquids. A hybrid approach in which parameterization using the forces, stresses and energies extracted from *ab initio* calculations uses DFT to generate a classical interatomic force field shows promise (Tangney and Scandolo, 2002). The hybrid approach fills in a void between purely FPMD and EPPMD methods. In this study we show that Ca, Al, Si and O self-diffusivities, melt shear viscosity and melt structures based on laboratory experiments agree reasonably with those computed from EPPMD simulations using relatively crude interatomic potentials.

3.2. Effective Pair Potentials

Effective pair-wise-additive ionic potentials that allow for partial charges, Coulombic long-range forces, Born electron repulsion, dipole–dipole Keesom forces, dipole-induced dipole Debye forces and London dispersion forces (grouped collectively as van der Waals forces) are employed here. Effective pair potentials are modifications of the actual (but unknown) pair interaction potential energy $V(r_{ij})$ that include the effects of all other atoms on the pair *ij* interaction, approximately (see Gray and Gubbins, 1984; March and Tosi, 1984 for discussion of potential energy functions). The general expression for the pair potential energy between two atoms *i* and *j* is:

$$V(r_{ij}) = \frac{q_i q_j e^2}{4\pi\varepsilon_o r_{ij}} + A_{ij}\exp\left(-\frac{r_{ij}}{B_{ij}}\right) - \frac{C_{ij}}{r_{ij}^6} \quad (1)$$

where q_i, q_j are the effective charges on species *i* and *j*, r_{ij} is the distance between the pair *ij*, *e* is the charge of the electron (1.60218×10^{-19} C), ε_0, is the vacuum permittivity (8.8542×10^{-12} C^2 m^{-1} J^{-1}), A_{ij} and C_{ij} are energy parameters for the pair *ij* describing repulsive and van der Waals attractive forces, respectively and B_{ij} is a *e*-folding length characterizing the radially symmetric decay of electron repulsion energy between atom pair *ij*. The parameters used in this study to model molten $CaAl_2Si_2O_8$ are identical to those used by Nevins and Spera (1998); the potential interactions of Si–O, Al–O, Ca–O and O–O are pictured in Fig. 1. This potential utilizes formal ionic charges of +2 for Ca, +4 for Si, +3 for Al and −2 for O and sets all van der Waals interaction to zero. In a later contribution, we compare results of this potential to those using the transferable potential developed by Matsui (1998) for compositions in the system Na_2O–CaO–MgO–Al_2O_3–SiO_2. The Matsui NCMAS potential uses fractional charges and includes non-zero van der Waals terms.

3.3. Molecular dynamic simulations

In this section, a brief description of the methods used is presented. The books Hanson and McDonald, 1986, Allen and Tildesley (1987), Haile (1992), Dove (1993), Hinchliffe (2000), Frenkel and Smit (2002) and Rapaport (1995) describe the methods, limitations and successes of MD

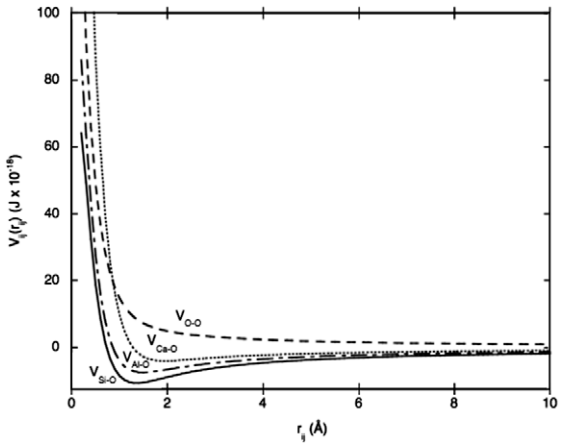

Fig. 1. Pair potential energies for Si–O, Al–O, Ca–O and O–O interactions computed from Eq. (1) in text. Numerical values of A_{ij} and B_{ij} are identical to those reported in Nevins and Spera, 1998.

modeling. In the geochemical literature, the reviews of Wolf and McMillan (1995), Poole et al. (1995) and Garofalini (2001) are especially useful. Earlier Molecular Dynamics results for geochemical systems by the UCSB group may be found in Rustad et al. (1990, 1991a,b,c), Stein and Spera (1995, 1996), Bryce et al. (1997, 1998), Nevins and Spera (1998) and Morgan and Spera (2001a,b). These studies were done on systems of $N \approx 1000$ atoms whereas in the current series of studies, $N \approx 10^4$. Recently the compositions Mg_2SiO_4 and $MgSiO_3$ have been studied by MD simulation (Martin et al., 2009; Nevins et al., 2009) using procedures identical to those used here. The studies of Guillot and Sator (2007a,b) and Lacks et al. (2007) provide additional EPPMD results for geochemical systems.

3.3.1. MD simulation methodology

The Large-scale Atomic/Molecular Massively Parallel Simulator (LAMMPS, see http://lammps.sandia.gov/) code described in Plimpton (1995) has been modified for use in geochemical systems to run efficiently on machines presently available. Details of the code and its implementation in a parallel environment on multiprocessor machines are provided in Nevins (2009). The code has been optimized to generate output needed for investigating geomaterials and for post-production analysis including coordination statistics and the efficient retrieval of thermodynamic and transport properties. The total simulation time for the work reported here is ~70 ns.

The essence of the MD computation is to find the vector sum of all forces acting on each particle due to every other particle within the MD primary cell utilizing Eq. (1). In detail, the force calculation is broken into long-range and short-range contributions. Two cut-off distances, one for Coulombic forces and another for Born and van der Waals forces are chosen and used to compute short-range forces directly. The computational work for the short-range calculation scales as N^2. Long-range Coulombic forces of the Ewald sum are computed by the Particle–Particle Particle–Mesh (PPPM) method (Darden et al., 1993). This algorithm scales as $N \log N$ and represents a significant computational savings compared to the classical Ewald sum, which scales as $N^{1.5}$ to N^2 depending on its precise implementation. Because the PPPM scales as $N \log N$, large particle simulations can be routinely accomplished thereby lowering the magnitude of statistical errors involved in the determination of physical properties from atom trajectories and time-correlation functions. The simulations are run keeping the number of particles (N), sample volume (V) and total energy (internal energy, E) of the system constant. This ensemble is called the microcanonical or NEV ensemble and corresponds to an isolated thermodynamic system. The internal energy represents the sum of the potential and kinetic energies, $E = E_P + E_K$. Once forces for each particle have been resolved, Newton's equations of motion are solved using a time step of 1 femtosecond (1 fs) using the Verlet (1967) scheme to advance the positions of all atoms. Serial application of the Verlet scheme generates atom trajectories (position and velocity) of all particles for a finite period of time; typically about 50–100 picoseconds (ps) for tracer diffusion and EOS studies and up to 5 nanoseconds (ns) for shear viscosity determinations. As typical in MD studies, periodic boundary conditions are used with the minimum image convention. In all the numerical experiments reported on in this paper, the total number of atoms used to simulate $CaAl_2Si_2O_8$ is $N = 6500$; in particular, $N_{Ca} = 500$, $N_{Al} = N_{Si} = 1000$ and $N_O = 4000$. In order to test the effect of cut-off distance, two NEV simulations were carried out under identical conditions except that the cut-off was increased from 0.6 nm to 1.2 nm. The results for melt of density 3367.49 kg/m^3 were: $T = 3583 \pm 31$ K, $P = 21.24 \pm 0.38$ GPa, $E = -41769.93$ kJ/mol and $T = 3570 \pm 31$ K, $P = 21.63 \pm 0.37$ GPa and $E = -41771.39$ kJ/mol, respectively. The short-range cut-off used in all production simulations was 0.6 nm, a good trade-off between accuracy and computational cost. The internal energy uncertainty associated with the cut-off is 1.3 kJ/mol, well within calorimetric uncertainty (Ghiorso, 2004a). Because we are interested in equilibrium liquid $CaAl_2Si_2O_8$ and not glassy $CaAl_2Si_2O_8$ (see Morgan and Spera, 2001a,b for MD studies on glassy $CaAl_2Si_2O_8$ using the same potential) simulation temperatures must remain $>\sim$3000 K at low pressure in order to insure ergodicity. At higher pressure, the computer glass transition temperature (T_g) is higher; performing simulations at $T < T_g$ is not appropriate for liquid thermodynamics.

3.3.2. Simulation protocol

The calculation at a given state point is carried out as follows. An appropriate number of atoms of each type are placed in the primary MD cell using the scheme of Refson (2000). The volume of the primary cell is fixed to give the desired melt density consistent with the number of atoms used in the simulation. The simulation is broken into a pre-production and production phase. Pre-production begins by setting a temperature of 10,000 K and allowing the system to equilibrate for 10 ps to obtain a Maxwellian distribution of velocities and constant total energy. Net momentum is then removed from the system. Temperature reduction is accomplished in 500 K steps by means of velocity rescaling. At each temperature, the system is allowed to relax for 5 ps to allow for thermal equilibration. When the desired run temperature is reached velocity rescaling is turned off and the system is equilibrated for an additional 10 ps and the temperature time series is statistically examined to insure thermal equilibrium. The criterion is that the average temperature and average pressure of the first 3 ps of the 10 ps record be statically identical to the average temperature and average pressure of the last 3 ps of the 10 ps interval. When thermal equilibration is achieved, a production simulation of 50 ps is made at the specified density and target temperature. Each production run is then checked for equilibrium by comparing the average temperature of the initial and the final 10 ps of the 50 ps production run. Results are not accepted unless the difference in these average temperatures (and pressures) is less than the one-sigma fluctuation σ_T and σ_p of the 50 ps production simulation. In the rare cases when this criterion is not met, the production run length is doubled to 100 ps and the last 50 ps are checked for thermal equilibration using the same criterion. All of the results presented in this series

of works are for equilibrium or metastable liquids unless otherwise noted.

4. RESULTS

4.1. Thermodynamic properties

Seventy-two MD simulations of (equilibrium or metastable) $CaAl_2Si_2O_8$ liquid have been carried out along twelve isochors spanning the melt density range 2398–4327 kg/m^3. Pressure and temperature span the range, 0.84–120 GPa and 3491–6102 K, respectively. Thermodynamic properties at each of the state points of the MD simulations are available in electronic annex; primary simulation results are presented in EA-1 and derived quantities are given EA-2.

4.1.1. Thermal pressure coefficient

The location of seventy-two state points along the twelve isochors is depicted in Fig. 2. Values of the thermal pressure coefficient (TPC),

$$\left(\frac{\partial P}{\partial T}\right)_V = \frac{\alpha}{\beta} \tag{2}$$

where α is the isobaric expansivity, $\alpha(P,T) \equiv \rho^{-1}(\frac{\partial \rho}{\partial T})_P$ and β is the isothermal compressibility, $\beta(P,T) \equiv -\rho^{-1}(\frac{\partial \rho}{\partial P})_T$ as a function of melt density are collected in EA-2. These values are taken directly from the raw MD simulations. The continuous curves in Fig. 2 represent the TPC along isochors derived from the EOS developed in Part II (Ghiorso et al., 2009). The derived EOS evidently provides an excellent representation of the thermal pressure coefficient. The TPC increases by an order of magnitude as density increases from 2398 kg/m^3 to 4327 kg/m^3 but is a weak function of temperature along an isochore. Across the pressure interval of the Earth's mantle, pressure produces a far larger effect on the TPC than temperature.

4.1.2. Isothermal compressibility and isobaric expansivity

MD simulations were carried out at six target temperatures from 3500 K to 6000 K along each isochore. Because the standard deviation of the average run temperature (≈27 K) for each target isotherm is smaller than the average temperature fluctuation of all MD simulations (≈38 K; see EA-1 electronic annex for values of σ_T), the isothermal compressibility can be computed from its definition directly using the MD results. Centered finite differences were used to calculate the isothermal compressibility at each state point except for the limiting isochors (2398 kg/m^3 and 4327 kg/m^3) for which forward differences are required. Values reported in EA-2 vary from 0.06 GPa^{-1} at 3533 K and 0.84 GPa to 0.002 at 6100 K and 120 GPa. Couched in terms of the isothermal bulk modulus, $K_T = \beta_T^{-1}$, values vary by a factor of 30 from ~17 GPa to 503 GPa. The large variation in bulk modulus with pressure is consistent with the models of Bottinga (1985) who suggested that compressibility variations in the Al-rich silicate melts $NaAlSi_2O_6$ and $Mg_3Al_2Si_3O_{12}$ are related to changes in melt structure at high pressure. In the case of $CaAl_2Si_2O_8$, the variation in isothermal compressibility correlates with the formation of silicon and aluminum pentahedrally coordinated by oxygen ($SiO^{[5]}$ and $AlO^{[5]}$) in distorted non-corner-sharing trigonal bipyramids, the destruction of silica and alumina tetrahedra and the formation of Si, Al octahedra as pressure increases (see below).

Once $\beta_T(P, T)$ is known, the isobaric expansivity $\alpha(P, T)$ can be computed from the thermal pressure coefficient and the compressibility. Computed values of the isobaric expansivity are collected in electronic annex EA-2. The highest value, 5.6×10^{-5} K^{-1} is found at $\rho = 2600$ kg/m^3, 3551 K and 2.3 GPa whereas the smallest value, 1.1×10^{-5} K^{-1} occurs at 6102 K and 120 GPa. A 'typical' value for the isobaric expansivity of molten $CaAl_2Si_2O_8$ in the range 3500–6000 K and 0–120 GPa is 2.7×10^{-5} K^{-1}.

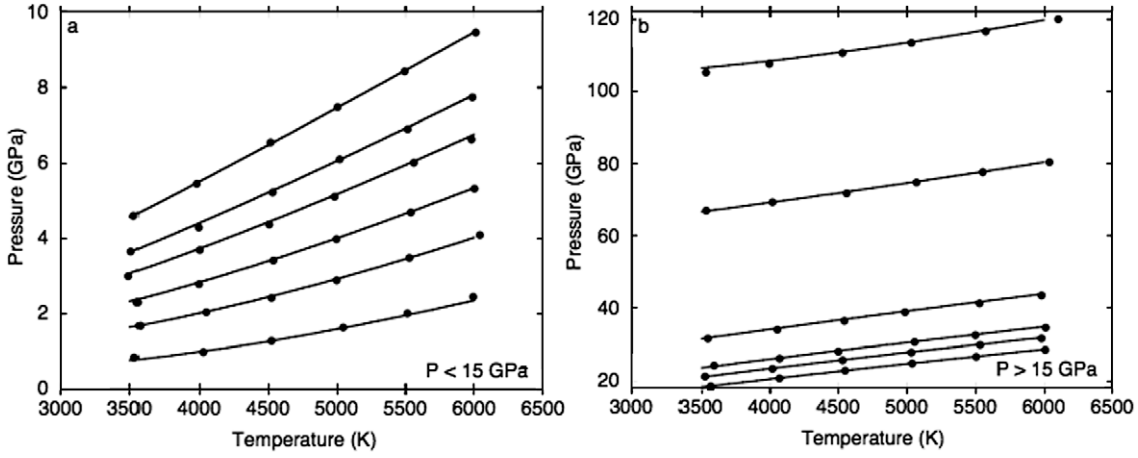

Fig. 2. Pressure–temperature plot showing location of all state points (closed circles) along the 12 isochores investigated by MD simulation. The slope of the isochore gives the thermal pressure. The continuous curves are fits to the raw MD data taken from Part II (Ghiorso et al., 2009). In all cases the derived EOS fit is an excellent representation of the raw MD results.

4.1.3. Internal energy, isochoric heat capacity and Grüneisen parameter

The molar internal energy is the sum of the potential and kinetic energies, $E = E_P + E_K$ and is computed at each production simulation time step and then averaged over all steps to give the values for a state point (electronic annex EA-1). In general, $E_P >> E_K$; in particular E_K is about 2–3% of the total energy. For a classical ionic material, the kinetic energy is

$$E_k = \frac{3}{2} n \mathscr{R} T \tag{3}$$

where $\mathscr{R}$ is the universal gas constant and n is the number of atoms in one formula unit of the substance ($n = 13$ for $CaAl_2Si_2O_8$). Comparison of values in Table 1 with Eq. (3) is excellent with a difference of less than 0.1%. Values of the molar potential energy (E_P) have been used to test the fundamental-measure free energy functional form for the liquid Madelung energy proposed by Rosenfeld and Tarazona (1998). In RT scaling the temperature dependence of the molar potential energy is given by

$$U_P = a(V) + b(V) T^{3/5} \tag{4}$$

where $a(V)$ is the Helmholtz free energy at 0 K. Both the 'a' and 'b' are functions of volume alone. MD data were used to test Eq. (4) and are shown in Fig. 3. If RT scaling was exactly obeyed, U_P would fall along linear arrays when plotted against $T^{3/5}$ since V is constant along an isochore. The fit of the data to the RT scaling expectation is excellent (see Part II for extended discussion). Combination of Eqs. (3) and (4) gives for the molar internal energy

$$E(V,T) = a(V) + b(V) T^{3/5} + \frac{3}{2} n \mathscr{R} T \tag{5}$$

Values for the functions $a(V)$ and $b(V)$ are given in Part II (Ghiorso et al., 2009).

The derivatives of the molar internal energy $E(V, T)$ may also be computed. The volume derivative of the internal energy is computed from the coordinates of the state point and the thermal pressure coefficient,

$$\left(\frac{\partial E}{\partial V}\right)_T = T\left(\frac{\partial P}{\partial T}\right)_V - P \tag{6}$$

and is given in EA-2. A strong negative dependence on density is noted with little temperature dependence. The isochoric heat capacity $C_V \equiv \left(\frac{\partial E}{\partial T}\right)_V$ has been computed by two methods. The fluctuations in U_K in the microcanonical (NEV) ensemble allows one to compute C_V at each state point by the expression

$$C_V = \frac{3k_B}{\left(1 - \frac{3N(\langle U_K^2\rangle - \langle U_K\rangle^2)}{3k_B^2 T^2}\right)} \tag{7}$$

Table 1
Self-diffusion fit parameters for Arrhenian Eq. (13) in text.

Species	D_0 (m^2/s)	E^* (kJ/mol)	V^* (cm^3/mol)	r^2 correlation coefficient
Ca	3.80×10^{-7}	176.5	1.57	0.926
Al	3.89×10^{-7}	183.6	1.45	0.947
Si	3.25×10^{-7}	187.9	1.41	0.954
O	3.98×10^{-7}	169.7	0.81	0.979

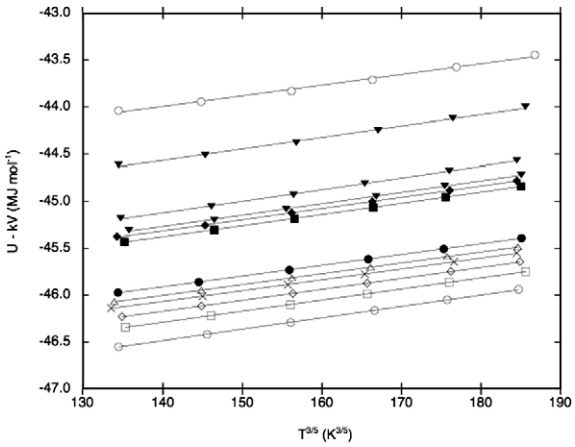

Fig. 3. Test of the Rosenfeld–Tarazona (RT) scaling relation for the Madelung energy (U_P) of the melt as a function of temperature. The kV term is introduced to make the plot more legible. V is the constant molar volume along a particular isochore and k is an arbitrary constant equal to 1 MJ/mol m^3. RT scaling predicts the MD data will fall along a straight line; evidently RT scaling is an excellent approximation for molten $CaAl_2Si_2O_8$ described by the potential used in this study.

where the brackets represent an average over all time steps of the equilibrium MD simulation (i.e., the production simulation). A disadvantage of this method is the fluctuations in U_K will lead to fluctuations in C_V. A second method to compute C_V less susceptible to statistical fluctuations is to compute finite differences along isochores. Values for C_V computed by the second method are given in EA-2. These show that C_V decreases along an isochore as P and T increase.

Finally, Grüneisen's parameter

$$\gamma = \frac{\alpha V}{\beta C_V} \tag{8}$$

where V is molar volume and C_V the molar isochoric heat capacity of liquid $CaAl_2Si_2O_8$ can be computed. Values are collected in EA-2. The Grüneisen parameter is virtually independent of temperature and depends linearly on density in the range 2400–3500 kg/m^3. At density greater than about 3500 kg/m^3, γ becomes nearly constant and approaches unity.

4.2. Coordination statistics and melt structure

Nearest neighbor distributions encapsulate short to medium-range order (Ziman, 1972) in a liquid and enable the connection between atomic structure and material properties to be understood, at least to first-order. Short-range nearest neighbor structure is determined by statistical analysis of atom locations using partial pair correlation functions (radial distribution functions, RDF) expressed,

$$g_{ij}(r) = \frac{V}{N^2}\left\langle \sum_{i=1}^{N} \sum_{j=1, i\neq j}^{N} \delta(r - r_{ij}) \right\rangle \tag{9}$$

For atoms i and j, Eq. (9) gives the normalized averaged distribution of atom i around a central j atom within a defined cut-off distance. V is the volume of the MD primary

cell and N the number of particles. The brackets denote averaging. Numerical integration of the RDF determines the coordination number for atom i around atom j based on locating the distance of the first minimum in the ij-pair RDF, $g_{ij}(r)$, following the first maximum. This cut-off distance is uniquely determined at each state point. An archive of nearest neighbor distributions of all atoms around all other atoms at each state point is presented in electronic annex EA-3. Here, the focus is on the statistics of Ca, Al, Si and O around a central O and of O around central Si, Al and Ca. For the range of P–T conditions investigated, T varies by a factor of ~2 (3500–6000 K) whereas P varies by a factor of 10^2 (1–10^2 GPa). It follows, given typical values of α and β that pressure is the dominant variable affecting melt density and hence structure in the P–T range of this study. Overall the effects of temperature are relatively muted compared to the dramatic effects of pressure. Accordingly, we present a detailed discussion of the coordination statistics at 3500 K isotherm and follow with a brief discussion of the differences in coordination environments between 3500 K and 6000 K. We adopt the notation $AB^{[n]}$ where n is the number of B atoms that are nearest neighbors to a central A atom. For example, a silicon octahedrally coordinated by oxygen is written $SiO^{[6]}$ and an oxygen tetrahedrally coordinated by four other oxygen atoms is written $OO^{[4]}$.

4.2.1. Coordination of Si, Al, Ca and O around oxygen

By mass, number fraction and volume $CaAl_2Si_2O_8$ is dominated by oxygen and therefore the coordination statistics of Si, Al, Ca and O around central oxygen are examined in detail. As pressure increases the average coordination of Si around oxygen increases from 1.1 to 1.6 (EA-3 and Fig. 4a). In particular, the concentration of oxygen with one or two nearest neighbors of silicon ($OSi^{[0]}$ or $OSi^{[1]}$, respectively) decreases whereas oxygen with two nearest Si neighbors ($OSi^{[2]}$) and $OSi^{[3]}$ (the latter as in stishovite) increase as pressure is raised. For Al, similar trends are

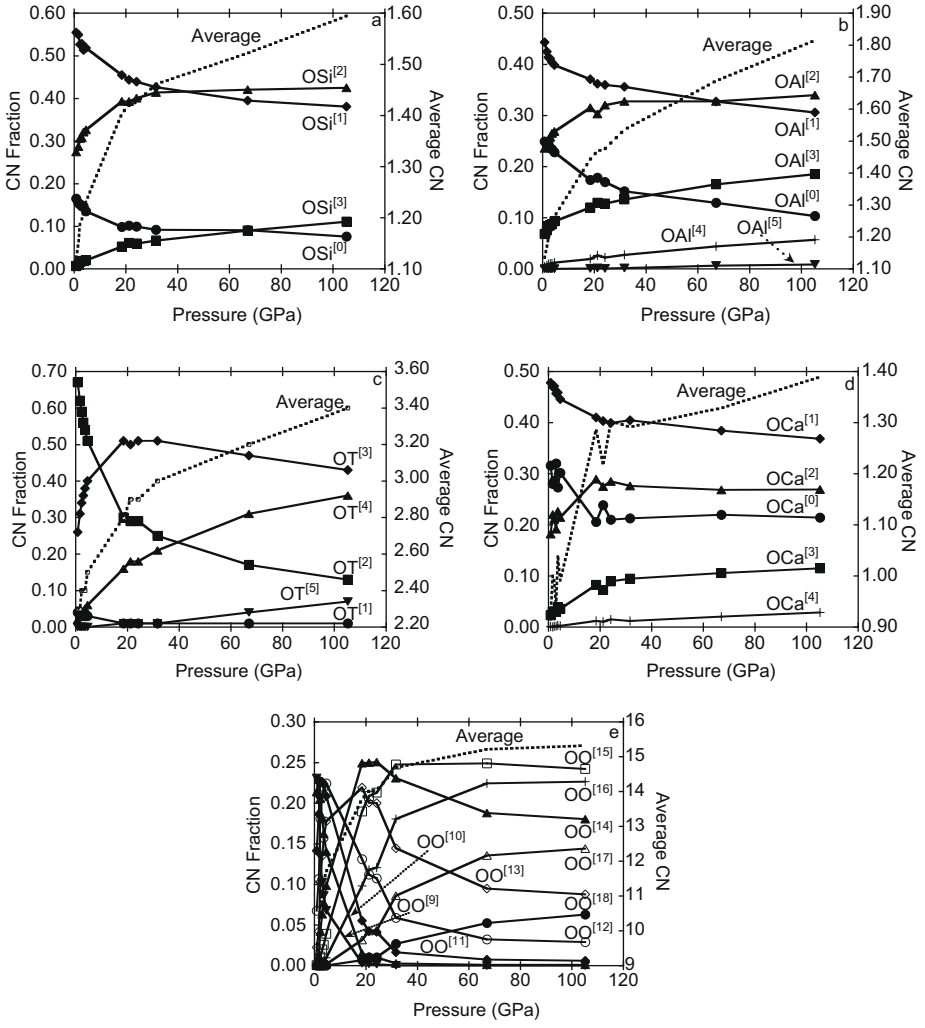

Fig. 4. Coordination statistics at 3500 K as a function of pressure for Si, Al, Ca and O around central O. The notation used to describe coordination polyhedra is $AB^{[n]}$ where n is the number of B atoms that are nearest neighbors to a central A atom. (a) Coordination of silicon around central oxygen. (b) Coordination of Al around central O. (c) Coordination of T around central oxygen. T represents either Si or Al atom. $OT^{[1]}$ is equivalent to non-bridging oxygen, NBO. (d) Coordination of Ca around central O. (e) Coordination of O around central O.

found (Fig. 4b) except that at any given pressure more of the Al is in high coordination with O relative to Si at the same pressure or density. In particular, the average CN of Al around O increases from ~1.2 to 1.8 from low pressure to 110 GPa. In order to study the linkages between AlO_n and SiO_n polyhedra and hence the intermediate range structure, it is useful to define the 'fictive' component T that represents *either* silicon or aluminum. In Fig. 4c, T–O statistics are depicted. Non-bridging oxygen ($OT^{[1]}$) is present in low concentration (~5%) at low pressure and disappears as pressure increases. The presence of $OT^{[1]}$, or non-bridging oxygen (NBO), is consistent with the NMR spectroscopic data of Stebbins and Xu (1997) on glassy $CaAl_2Si_2O_8$. These authors found ~5 mol% NBO in $CaAl_2Si_2O_8$ glass quenched from high temperature at 1 bar, essentially the same as found here in the liquid at circa 0.8 GPa and 3500 K. Most oxygen (~65%) has two nearest T neighbors at low pressure, consistent with a high degree of polymerization define by the sharing of oxygen between TO_4 tetrahedra. Recall that in crystals of anorthite all Si and Al are in twofold coordination with oxygen. As pressure rises, twofold T decreases, tricluster oxygen coordinated by Si or Al ($OT^{[3]}$) attains a maximum at circa 20 GPa and oxygen with four nearest neighbors of either Si or Al (i.e., $OT^{[4]}$) increases monotonically. The increase in shear viscosity of molten $CaAl_2Si_2O_8$ with increasing pressure (see below) correlates very well with the decrease in bridging oxygen ($OT^{[2]}$) and increase in tricluster and fourfold oxygen depicted in Fig. 4c.

Ca around O shows similar variation with pressure (EA-3 and Fig. 4d) although an average Ca is surrounded by slightly fewer oxygens compared to Si and Al, a feature consistent with the larger effective radii of Ca compared to Si and Al. In detail, there is a decrease in concentration of oxygen with no ($OCa^{[0]}$) or one ($OCa^{[1]}$) nearest Ca neighbor and a concomitant increase in $OCa^{[2]}$ and tricluster $OCa^{[3]}$ (i.e., oxygen with three nearest Ca neighbors) in the pressure interval 0–20 GPa. The net effect is an increase in the mean CN of Ca around O from less than unity to ~1.4 at high pressure.

Finally, the distribution of O around O – the topology of the oxygen sub-lattice – is portrayed in Fig. 4e. The average coordination number ($\overline{CN}$) of oxygen around oxygen is ~9 at low pressure and rapidly increases in the pressure interval $0 < P < 20$ GPa to ~15. There is an especially rapid increase in the range 0–5 GPa, the same pressure interval in which the concentration of SiO_5 and AlO_5 polyhedra maximize. $\overline{CN}$ attains a broad plateau around 15 for pressure in the range 40–60 GPa. There is evidently a profound reorganization of the rate of change of the oxygen sub-lattice for $0 < P < 20$ GPa that is largely complete by ~20 GPa. In Part II (Ghiorso et al., 2009) this is the approximate pressure at of the transition from the low-P to high-P EOS.

4.2.2. Coordination of O around Si, Al and Ca

The coordination of oxygen around Si, Al and Ca is depicted in Fig. 5a–c. $\overline{CN}$ of O around Si increases from ~4.4 to 6.4 with the most rapid change occurring 0–20 GPa (EA-3; Fig. 5a). $SiO^{[4]}$ (Si fourfold coordinated by oxygen) decreases monotonically with increasing pressure and is virtually absent by 20 GPa. In contrast, $SiO^{[5]}$ attains a maximum at ~5 GPa with an abundance of 60% and thereafter decreases; its abundance is ~30% at 30 GPa. From Fig. 5, the rate of change in abundance of $SiO^{[5]}$ is quite

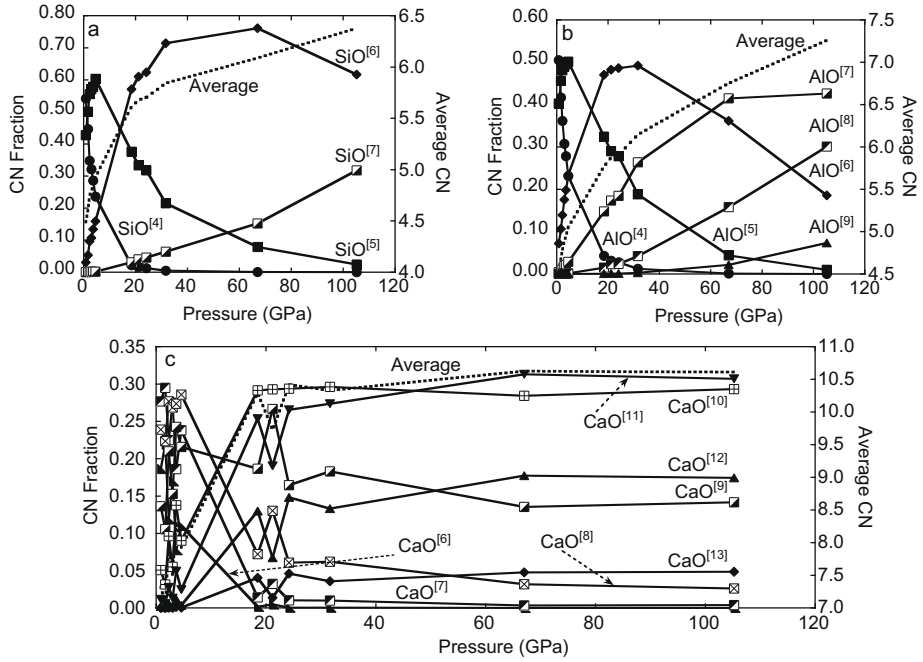

Fig. 5. Coordination statistics at 3500 K as a function of pressure for oxygen around central Si, Al and Ca. (a) Coordination of oxygen around central silicon. (b) Coordination of oxygen around central Al. (c) Coordination of oxygen around central Ca. Note the especially rapid structural changes at $P < 20$ GPa (see text for discussion).

large at low pressure. Inaccuracies of the potential might be responsible for the rather high abundance of predicted pentahedral Si at low pressure. ^{29}Si MAS NMR spectral studies by Stebbins and Poe (1999) on a $CaSi_2O_5$ glass quenched from a liquid at 2600 K and 10 GPa demonstrated, in fact, the presence of $SiO^{[5]}$ and $SiO^{[6]}$ although at lower (~3%) concentration than found in the calcium aluminosilicate composition studied here. Study is currently underway using the transferable potential of Matsui (1998) to test the sensitivity of $SiO^{[n]}$ and $AlO^{[n]}$ abundances on the potential parameters. Additional laboratory studies including *in situ* measurements on calcium aluminosilicate liquids at high temperature and pressure are needed to quantitatively evaluate the abundance of pentahedral silicon and aluminum in liquid $CaAl_2Si_2O_8$ as a function of pressure at high temperature.

Silicon octahedrally coordinated by oxygen ($SiO^{[6]}$), initially absent, increases rapidly in abundance in the interval 0–20 GPa and attains a broad abundance maximum of 75% around 70 GPa. At the highest simulation pressure, octahedrally coordinated Si is the most abundant coordination state for Si (~70%) followed by $SiO^{[7]}$ (~30%).

The effect of pressure on the CN of O around Al is depicted in Fig. 5b. The average CN of O around Al increases from ~4.5 to ~7.3 across the pressure interval. The statistics of O around Al are similar to those for O around Si except that Al is more highly coordinated by O compared to Si at a given pressure. This is expected due to its greater effective size.

Finally, the coordination of O around Ca is displayed in Fig. 5c. Once again, $\overline{CN}$ changes rapidly in the interval 0–20 GPa increasing from ~7 to ~10. At pressure greater than 20 GPa, $\overline{CN}$ increases only slightly; at 110 GPa the $\overline{CN}$ of O around Ca is ~10.5.

4.2.3. *Effect of temperature on structure*

Figs. 6 and 7 are analogous to Figs. 4 and 5 and show coordination statistics at 6000 K. Comparison of coordination statistics between 3500 K and 6000 K indicates a small but noticeable effect. At 6000 K coordination

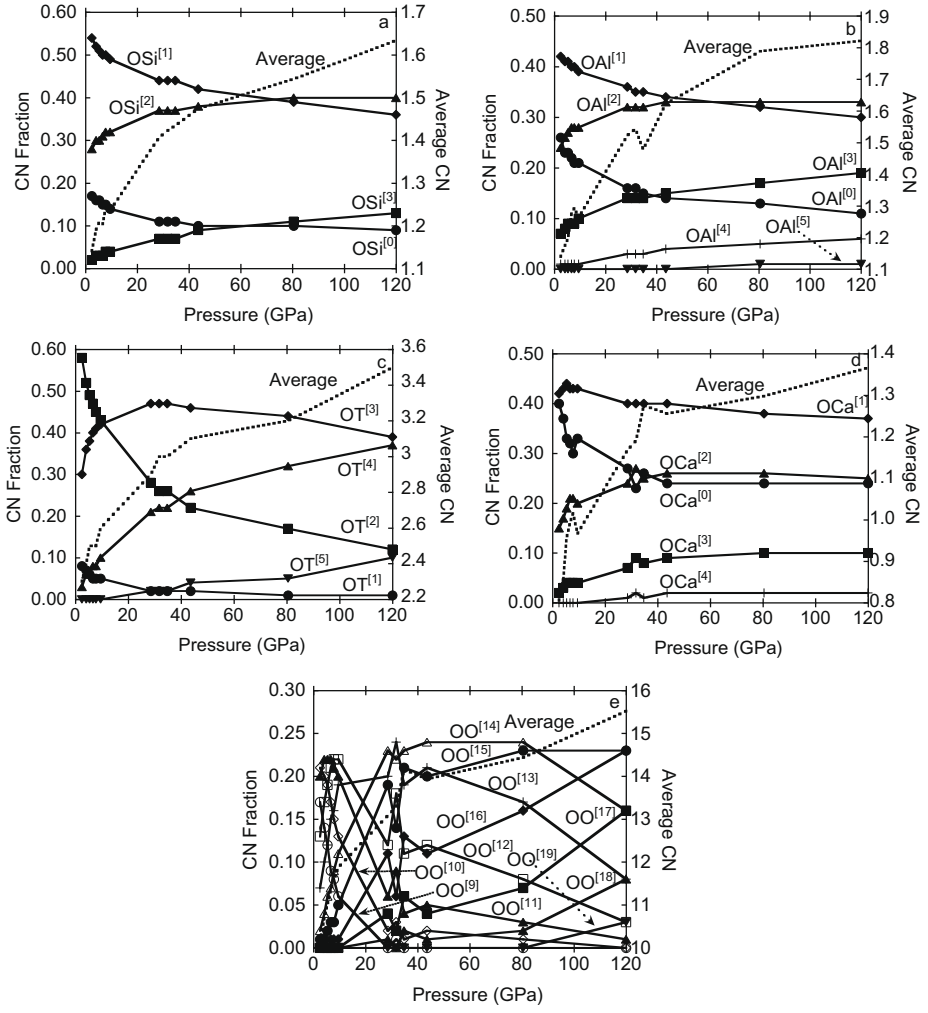

Fig. 6. Coordination statistics at 6000 K as a function of pressure for Si, Al, Ca and O around central O. (a) Coordination of silicon around central oxygen. (b) Coordination of Al around central O. (c) Coordination of T (either Si or Al) around a central oxygen. Note that $OT^{[1]}$ is equivalent to non-bridging oxygen, NBO. (d) Coordination of Ca around central O. (e) Coordination of O around central O.

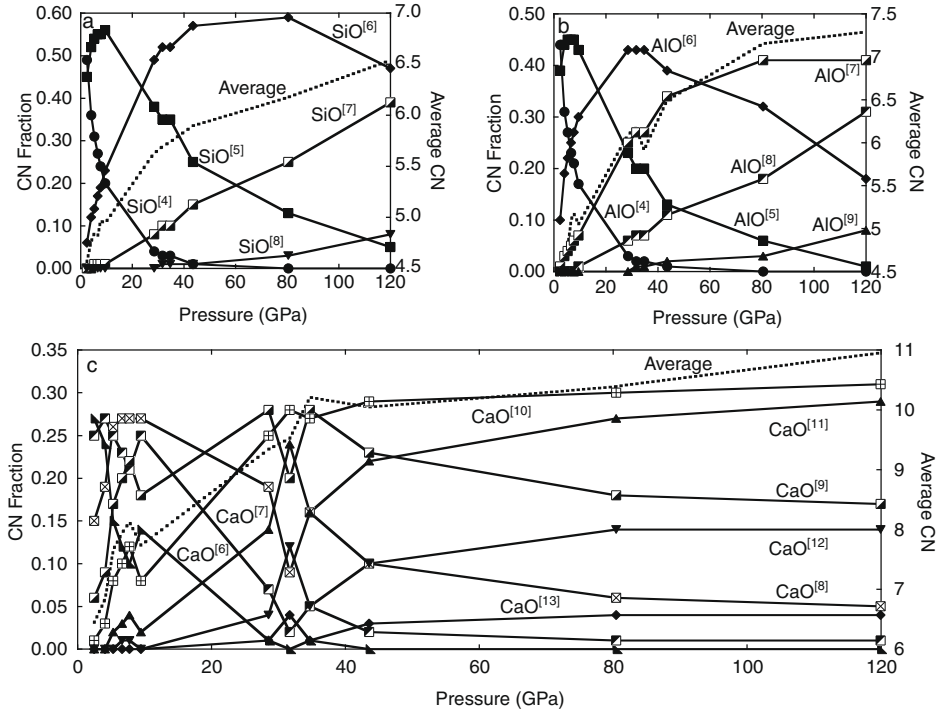

Fig. 7. Coordination statistics at 6000 K as a function of pressure for oxygen around central Si, Al and Ca. (a) Coordination of oxygen around central silicon. (b) Coordination of oxygen around central Al. (c) Coordination of oxygen around central Ca. Note the especially rapid changes in structure at $P < 20$ GPa.

number variations are related to those at 3500 K by providing an upwards 'shift' in the pressure of ~5–10 GPa. That is, a particular structural change (e.g., abundance of $SiO^{[4]}$ equal to 10% of total $SiO^{[n]}$ species) occurs at higher pressure at higher temperature. For example, Si and Al in fivefold coordination at 3500 K peak at 5 GPa and 4.6 GPa, respectively whereas at 6000 K the maxima occur at 10 GPa and 8 GPa, respectively (Fig. 7a and b). The abundances of tetrahedral Si and Al fall to 10% at 16 GPa and 18 GPa, respectively, at 3500 K whereas at 6000 K tetrahedral coordination is more abundant and shrinks to 10% of the total SiO_n and AlO_n at 25 GPa and 28 GPa, respectively. Similar differences are noted by examining the arrangement of oxygen around central Si or Al. For example, the abundance of oxygen's with one nearest Si neighbor equals the abundance of oxygen's with two nearest Si neighbors at about 40 GPa at 3500 whereas this same condition holds at about 70 GPa at 6000 K. At high temperature, the melt is slightly more depolymerized than at lower temperature. These systematic differences in melt structure as temperature increases can be modeled by equilibrium relations of the form $OT^{[1]} + OT^{[3]} \rightarrow 2OT^{[2]}$ (e.g., see Morgan and Spera, 2001b). In summary, although there are demonstrable changes in coordination as temperature increases at fixed pressure, the differences are modest compared to very dramatic changes in structure with pressure isothermally. The latter are very significant especially in the interval 0–20 GPa and essentially govern the change in transport properties of liquid $CaAl_2Si_2O_8$ as pressure increases (see below).

4.3. Self-diffusion of O, Si, Al and Ca

In a continuous system, the diffusion coefficient D is defined by combining Fick's first and second laws to give,

$$\frac{\partial C}{\partial t} = D\nabla^2 C \tag{10}$$

where $C(\mathbf{r}, t)$ is the local density or concentration of some atom. This result applies both to diffusion of one species through another and to self-diffusion. At the discrete particle level concentration C may be written in terms of the Dirac delta function, $\delta(r)$

$$C(\mathbf{r}, t) = \sum_{j=1}^{N_a} \delta(\mathbf{r} - \mathbf{r}_j(t)) \tag{11}$$

For large t, the Einstein expression (McQuarrie, 1976) for the Mean Square Displacement (MSD) is related to the diffusion coefficient by

$$D = \frac{1}{6N_a t}\left\langle \sum_{j=1}^{N_a} [\mathbf{r}_j(t) - \mathbf{r}_j(0)]^2 \right\rangle \tag{12}$$

where N_a refers to the number of atoms of species 'a' and the quantity in brackets represents the MSD of the ath atom type. Unfolded atomic trajectories are used in the calculation of the tracer diffusivity since periodic boundary conditions in the MD simulations imply a wraparound (Rapaport, 1995). At each state point, the MSD for a particular species (Ca, Si, Al and O) is accumulated from the unfolded atom trajectories and a plot of MSD versus time is made. Following a brief (<1 ps) ballistic transport

regime, the MSD average over all atoms of the same type becomes linear; the slope of the MSD is directly proportional to the self-diffusivity. Self-diffusivities at all state points have been computed and are collected in electronic annex EA-2; selected results and depicted in Fig. 8a–d where D is plotted versus pressure for 4000–5500 K. At low pressure ($P < 3$ GPa), $D_{Ca} \sim D_O > D_{Al} > D_{Si}$ with $D_{Ca}/D_{Si} \approx 3$–6. As found in the study of Nevins and Spera (1998; see their Fig. 7), self-diffusivities exhibit 'anomalous' behavior at low pressure ($0 < P < 2$ GPa) such that D *increases* as pressure increases. This is most apparent for Al, Si and O by examining very closely the very low-pressure region in Fig. 8, implying that activation volume is negative or that increasing pressure *increases* the volume of the activated region associated with self-diffusion at low pressure. This anomalous behavior is related to the observed coordination statistics at low pressure. In effect, the network of linked SiO_4 and AlO_4 tetrahedra breaks down rapidly in the P range 0–5 GPa and short-range order is dominated by the abundance of trigonal bipyramidal polyhedra (SiO_5 and AlO_5). At higher pressure, the tracer diffusivity magnitudes are ordered $D_O > D_{Ca} \approx D_{Al} \approx D_{Si}$ at all temperatures. Ca, Al and Si diffuse at similar rates whereas oxygen diffuses appreciably faster by about an order of magnitude at the highest pressure studied. The deviation between the oxygen diffusivity and that of Ca, Al and Si increases as pressure increases along an isotherm.

4.3.1. Temperature and pressure dependence of self-diffusivities

The simplest analytic form for the P–T variation of the self-diffusivity is the Arrhenian expression,

$$D(P,T) = D_0 \exp\left(\frac{-(E^* + PV^*)}{\mathscr{R}T}\right) \tag{13}$$

where D_0, the pre-exponential 'frequency factor', is the diffusivity in the limit $T \to \infty$, E^* is the activation energy for diffusion, V^* is the activation volume for diffusion and $\mathscr{R}$ is the universal gas constant. In Eq. (13), E^* and V^* are constant. Arrhenian parameters D_0, E^* and V^* for each species obtained from fitting the self-diffusivity values to Eq. (13) are given in Table 1. Activation energies lie in the narrow range 170–188 kJ/mol. The activation volume for oxygen $V^*_{oxygen} \approx 0.8$ cm^3/mol whereas for Ca, Al and Si, V^* is about twice as large ($\approx$1.4–1.6 cm^3/mol). A plot of log D versus P should be linear along an isotherm if the activation volume is strictly constant. Examination of Fig. 8 reveals that the derivative $(\frac{\partial \ln D}{\partial P})_T = \frac{-V^*}{\mathscr{R}T}$ decreases as pressure increases. The decrease in V^* as pressure increases is most noticeable at low temperature (e.g., 3500 K and 4000 K); at high temperatures, V^* varies more weakly with pressure although it clearly is not constant. We have therefore explored the consequences of allowing for variation of E^* and V^* with temperature, pressure or both by comparing correlation coefficients for the different models. It is easy to show that model expressions with $E^* = f(T)$, $E^* = f(P)$ or $E^* = f(P, T)$ do not produce functional deviations from the usual Arrhenian form (although the *numerical* values are different) and so are not considered further. This leaves four models to compare: $V^* =$ constant, $V^* = f(T)$, $V^* = f(P)$ and $V^* = f(P, T)$. We find that the statistically best form is with activation volume a linear function of pressure, $V^* = v_0^* + v_1^* P$. The self-diffusivity becomes

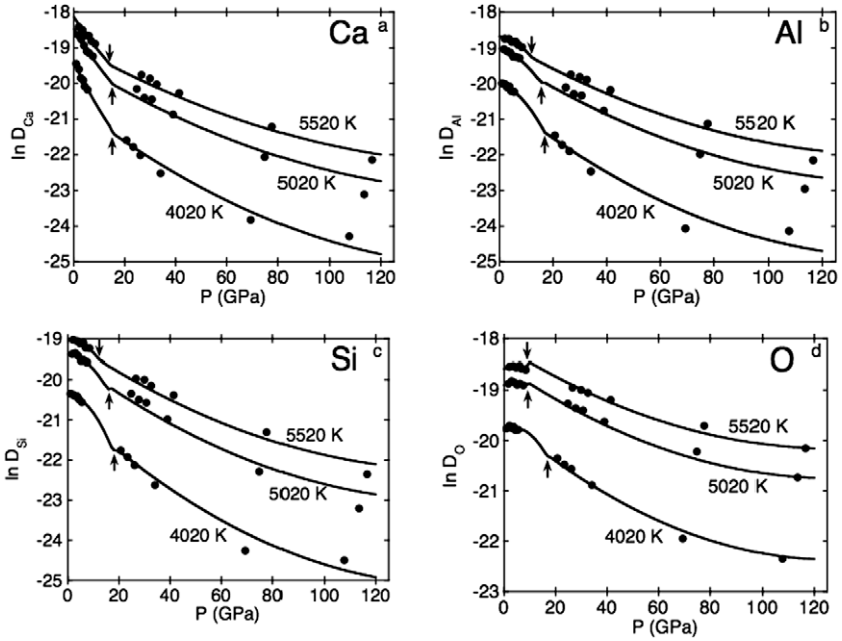

Fig. 8. Self-diffusivity of Ca, Al, Si and O as a function of pressure along three isotherms. Raw MD values plotted as filled circles. The arrows mark the boundary between the low pressure and high pressure Arrhenian fits and correspond to the pressure region where melt structure changes rapidly. Curves are based on parameters recorded in Table 3 for low-P and high-P fits. (a) Ca self-diffusivity at 4020 K, 5020 K and 5520 K. (b) Al self-diffusivity along isotherms. (c) Si self-diffusivity along isotherms. (d) Oxygen self-diffusivity along isotherms.

$$D = D_0 \exp\left(\frac{-[E^* + (v_0^* + v_1^* P)P]}{\mathscr{R}T}\right) \quad (14)$$

The constants for the model are listed in Table 2. Values for D_0 and E^* change slightly from the simple Arrhenian model, with E^* in the range 166–181 kJ/mol and D_0 values about 10% higher. The constant v_0^* represents the activation volume at zero pressure and ranges from a minimum of 1.3 cm^3/mol for O to 3 cm^3/mol for Ca, Si and Al are similar and equal to 2.5 cm^3/mol which is roughly 5–10% of the molar volume. The constant v_1^*, a measure of the pressure dependence of the activation volume, is negative for all atoms around -10^{-2} cm^3/mol GPa. This means that the volume of activation decreases with increasing pressure. The correlation coefficient (r^2) for the modified Arrhenian fit (Eq. (14)) is improved over the simple Arrhenian model (Eq. (13)).

An even better fit of diffusivity is achieved by recognizing the dramatic change in liquid structure taking place at low pressures. Fig. 8 shows the results of a model with low-P and high-P fits to the diffusion data. The pressure of the 'transition' depends upon the temperature and occurs in the 18–20 GPa range. This range is consistent with the dramatic changes in melt structure revealed by coordination statistics. Regression parameters are gathered in Table 3 for the low-P and high-P fits. High-pressure fits for all elements are characterized by higher activation energies and generally larger activation volumes. In particular, for the low-pressure fit both Si and oxygen exhibit so-called 'anomalous' diffusion where self-diffusivity *increases* as pressure *increases*, quite the opposite for 'normal' fluids. This anomalous behavior is associated with the negative activation volume at zero pressure recorded in Table 3. The anomalous region is subtle because the pressure interval on Fig. 8 is so large. The anomalous effect is easier to see on analogous plots in Nevins and Spera (1998) who found activation volumes around −25 to −35 cm^3/mol at zero pressure. At the atomic level, the anomalous behavior correlates with the very rapid decrease in the abundance of SiO_4 and AlO_4 polyhedra and the concomitant rapid increase in the abundance of SiO_5 and AlO_5 polyhedra in the range 0–5 GPa.

4.4. Comparison with laboratory diffusion results

There are no laboratory studies of self-diffusion in molten $CaAl_2Si_2O_8$ at the P–T conditions of the MD simulations. There are, however, some laboratory diffusion results on compositions and structures similar or analogous to molten anorthite and here we compare the MD-derived values with these laboratory results.

The calculated value of 166 kJ/mol for E^* for Ca (Table 2) may be compared to the laboratory result of Jambon (1980) of ~191 kJ/mol for tracer Na diffusion in $CaAl_2Si_2O_8$ glass at 900–1300 K and 10^{-4} GPa. It should be noted that the laboratory value corresponds to a temperature below the glass transition and therefore are not directly comparable to the MD values. Oishi et al. (1975) measured self-diffusion coefficients in a melt of composition $40CaO{\cdot}20Al_2O_3{\cdot}40SiO_2$ (wt%). For comparison, $CaAl_2Si_2O_8$ is $20CaO{\cdot}37Al_2O_3{\cdot}43SiO_2$. They found at 1600–1900 K the ordering $D_O > D_{Ca} > D_{Al} > D_{Si}$, identical to the one found here for molten $CaAl_2Si_2O_8$. They found an activation energy for tracer oxygen diffusion of about 210 kJ/mol which can be compared to the MD result of 166 kJ/mol. Extrapolating the laboratory results to 3500 K, diffusion coefficients for all atoms in their study are larger by about a factor of 100 compared to the MD results. This is the expected behavior in light of the much greater concentration of CaO and smaller concentration of Al_2O_3 in the composition studied by Oishi et al. (1975). Watson (1982) measured the diffusion of Ca in dry obsidian. Extrapolating his result at 10^{-4} GPa to 3500 K gives $D_{Ca} = 1.2 \times 10^{-10}$ m^2/s whereas the MD value at the same pressure and temperature is $D_{Ca} = 1.4 \times 10^{-9}$ m^2/s. Because of the difference in composition this comparison is semi-quantitative at best. LaTourrette et al. (1996) studied self-diffusion of Ca in a haplobasaltic melt. They found E^* for Ca of 172 kJ/mol which compares favorably with the MD result of 166 kJ/mol despite the difference in composition. Consistent with the low viscosity of haplobasalt liquid they found the pre-exponential term (D_0) to be about fifty times higher than D_0 in $CaAl_2Si_2O_8$ for Ca. Liang et al. (1996) measured self-diffusivities for a number of compositions in the system CaO–Al_2O_3–SiO_2 at 1 GPa and 1500 °C. The bulk composition closest to $CaAl_2Si_2O_8$ was $20CaO{\cdot}20Al_2O_3{\cdot}60SiO_2$ (wt%). They found the ordering of self-diffusivities to be $D_{Ca} > D_{Al} > D_O > D_{Si}$ which is similar to the MD results except for the reversal in magnitudes of O and Al. The self-diffusivities of Al, Si and O extrapolated from the MD results are 1.4×10^{-12} m^2/s, 0.9×10^{-12} m^2/s and 3.8×10^{-12} m^2/s, respectively, and may be compared to the laboratory values of Liang et al. (1996) of 2.3×10^{-12} m^2/s, 1.4×10^{-12} m^2/s and 4.7×10^{-12} m^2/s, for D_{Al}, D_{Si} and D_O. Mungall et al. (1999) measured the Ca tracer diffusivity in the haplogranitic bulk composition $4K_2O{\cdot}5Na_2O{\cdot}11Al_2O_3{\cdot}80SiO_2$ (wt%). Extrapolation of their

Table 2
Activation energies and volumes computed by regression of MD-derived diffusion and viscosity values. Numerical values for both E^* and V^* are given in rational units. In calculations, all quantities should be expressed strictly in SI units. r^2 refers to the correlation coefficient of the multiple linear regression. Activation volume for both diffusion and viscosity is a linear function of pressure, $V^* = v_0^* + v_1^* P$.

Self-diffusivity	D_0 or η_0 (m^2/s) or (Pa s)	E^* (kJ/mol)	v_0^* (cm^3/mol)	v_1^* (cm^3/mol GPa)	r^2 correlation coefficient
Ca	4.2×10^{-7}	166.2	3.04	$^{-}1.42 \times 10^{-2}$	0.979
Al	4.2×10^{-7}	175.7	2.57	$^{-}1.09 \times 10^{-2}$	0.981
Si	3.5×10^{-7}	180.7	2.44	$^{-}9.92 \times 10^{-3}$	0.982
O	4.1×10^{-7}	166.4	1.29	$^{-}4.62 \times 10^{-3}$	0.991
Viscosity	1.60×10^{-4}	150.0	2.78	$^{-}1.3 \times 10^{-2}$	0.985

Table 3
Activation energies and volumes computed by regression of MD-derived diffusion values. Numerical values for both E^* and V^* are given in rational units. In calculations, all quantities should be expressed strictly in SI units. r^2 refers to the correlation coefficient of the multiple linear regression. Activation volume for diffusion is a linear function of pressure, $v^* = v_0^* + v_1^* P$. Low-pressure and high-pressure fits are provided. Note the so-called anomalous behavior of Si and O at low pressures where the self-diffusivity increases as pressure rises along an isotherm.

Self-diffusivity	D_0 (m^2/s)	E^* (kJ/mol)	v_0^* (cm^3/mol)	v_1^* (cm^3/mol GPa)	r^2 correlation coefficient
Low-pressure fit					
Ca	3.93×10^{-7}	155.4	4.90	−0.046	0.997
Al	2.65×10^{-7}	162.2	0.79	0.115	0.998
Si	2.09×10^{-7}	167.3	−0.059	0.152	0.998
O	2.29×10^{-7}	151.0	−0.94	0.117	0.999
High-pressure fit					
Ca	5.04×10^{-7}	203.9	1.82	-5.45×10^{-3}	0.970
Al	5.73×10^{-7}	202.1	2.00	-6.71×10^{-3}	0.968
Si	4.80×10^{-7}	204.9	1.96	-6.50×10^{-3}	0.972
O	6.43×10^{-7}	178.9	1.45	-5.68×10^{-3}	0.996

laboratory result to 3500 K gives $D_{Ca} = 5 \times 10^{-9}$ m^2/s which may be compared to 1.4×10^{-9} m^2/s from this study. Dunn (1982) measured the self-diffusion of oxygen in melt of composition $40CaMgSi_2O_6 \cdot 60CaAl_2Si_2O_8$ at 10^{-4} GPa and found an activation energy E^* of 185 ± 25 kJ/mol which compares favorably to $E^* = 166$ kJ/mol found here. Extrapolating his laboratory results to 3500 K give $D_O = 2.3 \times 10^{-9}$ m^2/s which compares favorably to the MD value of $D_O = 1.4 \times 10^{-9}$ m^2/s. Note that the composition Dunn studied was less viscous than molten $CaAl_2Si_2O_8$. Baker (1992) measured the tracer diffusivity of Si in an anhydrous rhyolitic melt at 1 GPa and 1300–1600 °C. He found an activation energy for Si diffusion of 139 ± 40 kJ/mol consistent within laboratory uncertainty with the value of 181 kJ/mol found here. Ryerson and McKeegan (1994) found the activation energy for oxygen self-diffusion in crystalline anorthite to be 162 ± 36 kJ/mol which is comparable to 181 kJ/mol found here for E^*_{Si}. Finally, Poe et al. (1997) measured the pressure dependence of oxygen self-diffusion in molten albite at 2100 K. They found a value for the activation volume V^*_{oxygen} of 2.2 cm^3/mol at 5–16 GPa. This compares with the value of 1.3 cm^3/mol for oxygen from Table 3.

In conclusion, the lack of laboratory self-diffusion data for liquid $CaAl_2Si_2O_8$ makes direct comparison impossible. However, comparison with laboratory data for similar systems indicates good agreement with E^* in the range 160–200 kJ/mol for all atoms and pre-exponential values of order 10^{-7} m^2/s. Activation volumes are ~3 cm^3/mol for the metals and about half of that for oxygen at high pressure. At low pressure, both Si and O show anomalous behavior in accordance with laboratory studies on a related (dacitic) composition (Tinker and Lesher, 2001; Tinker et al., 2004). The activation volume for self-diffusion decreases for all atoms as pressure increases.

4.5. Shear viscosity

The shear viscosity was computed from the MD results using linear response theory embodied as the Green–Kubo (GK) relations. Shear viscosity is determined by studying the temporal decay of appropriate stress components (both off and on-diagonal; Rapaport, 1987). The Green–Kubo (GK) expression for the shear viscosity is given by integration of the stress (pressure) autocorrelation function,

$$\eta = \frac{V}{3kT} \int_0^\infty \left\langle \sum_{x<y} p_{xy}(t) p_{xy}(0) \right\rangle dt \quad (15)$$

where η is the shear viscosity, V is the system volume, T is the temperature, k is Boltzmann's constant, and p_{xy} refers to the xy component of the stress. In addition to p_{xy}, p_{xz} and p_{yz} the first normal stress differences ($p_{xx} - p_{yy}$) and ($p_{yy} - p_{zz}$) are also used to compute five independent estimates of shear viscosity. The reported viscosity at a given state point is the average of the five independent computed values following the method detailed in Nevins and Spera (2007). The parameters used to optimize the viscosity computation include a fairly long simulation duration (t_D) of 2 ns, a window width (t_W) of 2, 5, or 10 ps, and a time interval between the start of successive time windows (t_S) of 10 fs. The GK formulation utilizes a single summation that consolidates the contributions of all atoms into a single autocorrelation function. Alternative formulations based on particle displacement require translational invariance, an assumption violated in MD simulations utilizing periodic boundary conditions (Haile, 1992).

The shear viscosity of $CaAl_2Si_2O_8$ in the pressure range 2.1–77.8 GPa, temperature range 3987–5563 K and density range 2398–3772 kg/m^3 calculated by the Green–Kubo method is shown in Fig. 9. Plotted points represent the MD values whereas the curves represent fits to the Arrhenian relationship,

$$\eta = \eta_0 \exp\left(\frac{E^*_\eta + P[v^*_{\eta_0} + P v^*_{\eta_1}]}{\mathscr{R}T}\right) \quad (16)$$

where E^*_η is the activation energy for viscous flow, $\mathscr{R}$ is the universal gas constant and the activation volume for viscous flow is a function of pressure, $V^*_\eta(P) = v^*_{\eta_0} + v^*_{\eta_1}$. Note that Eq. (16) is analogous to Eq. (14). Calculated fit parameters are given in Table 3. Independent high- and low-P fits were not performed although careful inspection of Fig. 9

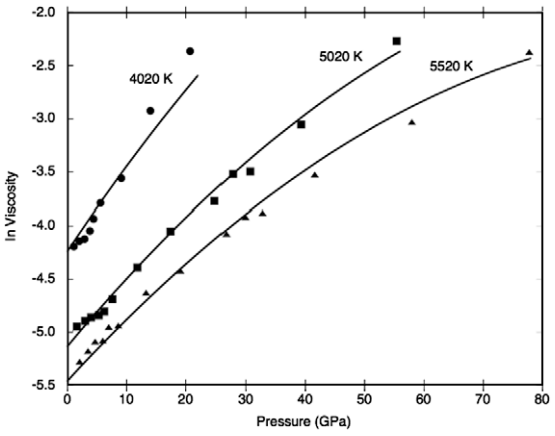

Fig. 9. Shear viscosity of liquid $CaAl_2Si_2O_8$ versus pressure along isotherms. Closed circles, filled squares and filled triangles represent MD-derived values at 4020 K, 5020 K and 5520 K, respectively. The curves are fits based on Eq. (16) and parameters in Table 2.

suggests that such a procedure could be justified although further MD simulations would be required to test this. The shallower slope at low pressure, especially at 4000–5000 K, suggests that melt viscosity depends less strongly on pressure at low pressure for $T < 4500$ K. This tendency is consistent with laboratory measurements of Kushiro (1981) and Taniguchi (1992). Although experimental data are at much lower T, they show that at very low pressure (0–2 GPa) melt viscosity is independent of pressure. At zero pressure Eq. (16) predicts a 1 bar shear viscosity of 3.2 Pa s compared to laboratory values in the range 5–15 Pa s. This is a reasonable agreement; a change in the activation energy of 10 kJ is sufficient to bring the MD results into agreement with laboratory measurements, themselves subject to considerable uncertainty. Predicted viscosity increases by a factor of 20, from 0.0043 Pa s to 0.091 Pa s at 5500 K as pressure increases from 1 bar to 80 GPa. At 3500 K, the estimated viscosity varies by a factor of ~120 (0.028 Pa s to 3.31 Pa s) for the same pressure range. The activation energy for viscous flow, 150 kJ mol^{-1}, is close to the activation energy for oxygen self-diffusion (166 kJ mol^{-1}) and suggests that oxygen mobility is key to understanding viscous flow. The zero-pressure activation volume for viscous flow of ~2.78 cm^3 mol^{-1} is close to the zero-pressure activation volume for Ca, Si and Al self-diffusion (2.4–3.0 cm^3 mol^{-1}) and about twice the value for oxygen self-diffusion (1.3 cm^3 mol^{-1}). The activation volume for viscous flow decreases by ~0.013 cm^3 mol^{-1} GPa^{-1} which is comparable to analogous self-diffusion parameters (coefficient v_1^*) recorded in Table 3.

4.6. Size of activated cluster for viscous flow and diffusion

Because independent values for the self-diffusivity and the shear viscosity are available from the MD simulations, the applicability of the Eyring relation can be addressed. Typically the Eyring or closely related Stokes–Einstein (SE) relation is used to estimate shear viscosity from self-diffusion data (or *vice versa*) by assuming a length scale ('size') of the atom or cluster of atoms involved in the activated process of atom mobility. Ambiguity generally arises, however, in selecting the 'size' of the activated cluster *a priori*. Here, we derive information regarding the nearest neighbor distribution and size of the diffusing unit based on MD-derived D and η values and compare these with liquid structures defined by coordination statistics. Lacks et al. (2007) have used this approach in MD studies on the binary $MgO–SiO_2$ at 3000 K and found that the SE relation works better than the Eyring relation in polymerized melts and *vice versa* in unpolymerized melts. Here we apply the Eyring relation to MD data covering a wide range in PT space and show how the size of the activated complex can be estimated.

The Eyring et al. (1982) formulation is based on an atomic level picture involving a jump of a particular atom (e.g., O, Si, Al or Ca) from one coordination environment to another. These environments can be characterized by a size related to the atom cluster involved in the diffusive event. The EY relationship between self-diffusivity and viscosity is

$$\xi(V/nN_A)^{1/3} = \frac{kT}{D\eta} \tag{17}$$

where n is the number of atoms per formula unit ($n = 13$), V is the P–T dependant molar volume, N_A is Avogadro's number and $\xi + 1$ is the number of atoms in the activated complex. The ratio $kT/\eta D_O$ defines a scale-length λ associated with the size of the 'activated cluster' involved in atomic mobility and viscous shear flow. In Fig. 10, $\lambda = kT/\eta D_O$ and ξ are is plotted for oxygen at 4000 K and 6000 K. At both 4000 K and 6000 K, λ decreases rapidly with pressure from around 18 Å (14–20 Å depending on T) at 1 bar to ~3.5 Å (2.5–5 Å depending on T) for $P >$ ~50 GPa. The number of atoms in the activated cluster changes from a ~7–9 at low pressure to a smaller activated unit of 2–3 atoms according to the Eyring relation. The rapid change in λ and ξ for $0 < P < 20$ GPa is consistent with the picture of melt structure, EOS and self-diffusion results presented earlier. The rapid reorganization of the melt from a '4–5' to a '6'-fluid takes place in the same pressure interval where the size of the activated complex shrinks appreciably.

5. CONCLUSIONS

Molecular dynamics simulations of molten $CaAl_2Si_2O_8$, a canonical network fluid, have been carried out at 72 state points spanning ranges in ρ (2398–4327 kg/m^3), T (3490–6100 K) and P (0.84–120 GPa) relevant to geosystems. Documentation of thermodynamic, transport and coordination statistics is presented in an electronic annex (EA-1, EA-2 and EA-3). The calculations enable a detailed examination of the coordination of Si, Al and Ca around central O as well as the coordination of O around central Si, Al, Ca and O as a function of P and T to study the relationship between melt structure and properties – both thermodynamic and transport – in liquid $CaAl_2Si_2O_8$. Melt structure

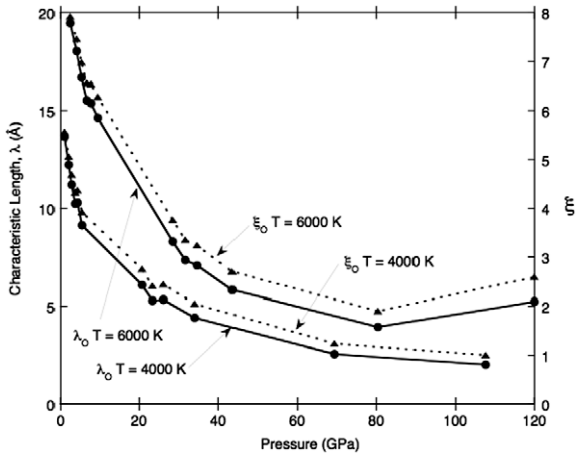

Fig. 10. Eyring plot based on oxygen diffusivity and Eq. (17). Characteristic length λ based on oxygen at 6000 K and 4000 K shows a strong dependence on pressure. At 4000 K for example, λ decreases from ~14 Å to ~3 Å. Right hand scale gives the nearest neighbor count of atoms surrounding a mobile oxygen. At 4000 K this varies from ~10 to ~1 as pressure increases from 0 GPa to ~100 GPa.

undergoes dramatic changes as pressure increases especially in the range 0–20 GPa. Pentahedrally coordinated Si and Al in distorted trigonal bipyramids attain abundance maxima of ~60% at 3–5 GPa and contrasts the behavior of rapidly decreasing $TO^{[4]}$ and rapidly increasing $TO^{[6]}$ polyhedra abundances. The coordination of oxygen around Ca and of oxygen around itself increases rapidly for $0 < P < 20$ GPa and increases less quickly at higher pressure. The proportion of non-bridging oxygen decreases whereas oxygen with two or three nearest neighbors of Si, Al or Ca increases as pressure increases. These dramatic changes in melt structure are reflected in the variation of thermodynamic, and transport properties of the liquid. The equation of state and variation of internal energy with T and V, used in Part II to derive a comprehensive thermodynamic description of liquid $CaAl_2Si_2O_8$, are best fit by allowing for EOS expressions broken into low-P ($P < 20$ GPa) and high-P ($P > 20$ GPa) intervals in accord with the atom coordination statistics. Values of the self-diffusivities of Ca, Al, Si and O are presented spanning the range of P and T of the MD simulations and are fit well by a modified Arrhenian expression in which the activation volume is a linear function of pressure only. Activation energies and volumes are computed for each atom and lie in the range 150–205 kJ/mol and 5 to -1 cm^3/mol depending on atom type and pressure range. A small pressure region exists for O and Si described by 'anomalous' diffusion. Self-diffusion values are best fit by 'low P' and 'high P' fits. Extrapolations of the MD-derived expressions compare reasonably with laboratory self-diffusivity measurements. Green–Kubo calculations for the shear viscosity of molten $CaAl_2Si_2O_8$ are presented enabling application of the Eyring model to determine the characteristic size and number of atoms in the activated cluster. The latter decreases from ~8 to ~3 from low to high pressure and provides additional insight into the mobility dynamics. Comparison of laboratory falling sphere viscosity values and MD-derived values is quite reasonable.

ACKNOWLEDGMENTS

This research was supported by an allocation of advanced computing resources from the National Science Foundation and the Office of Science of the US Department of Energy. The computations were performed in part on DataStar at the San Diego Supercomputer Center and Seaborg and Franklin machines at the National Energy Research Scientific Computing Center. We acknowledge support from NSF Grants ATM-0425059 (VLab) and DOE Grant DE-FG-03-91ER-14211 and the University of California Santa Barbara. The input from four anonymous reviewers is gratefully acknowledged.

APPENDIX A. SUPPLEMENTARY DATA

Supplementary data associated with this article can be found, in the online version, at doi:10.1016/j.gca.2009.08.011.

REFERENCES

Aasland S. and McMillan P. F. (1994) Density-driven liquid–liquid phase separation in the system Al_2O_3–Y_2O_3. *Nature* **369**, 633–636.

Abe Y. (1997) Thermal and chemical evolution of the terrestrial magma ocean. *Phys. Earth Planet. Inter.* **100**, 27–39.

Akins J. A., Luo S. N., Asimow P. D. and Ahrens T. J. (2004) Shock-induced melting of $MgSiO_3$ perovskite and implications for melts in Earth's lowermost mantle. *Geophys. Res. Lett.* **31**, 14.

Allen M. P. and Tildesley D. J. (1987) *Computer Simulation of Liquids*. Oxford University Press Inc., New York.

Anderson D. L. (2007) *New Theory of the Earth*. Cambridge University Press.

Asimow P. D. and Ahrens T. J. (2008) Shock compression of liquid silicates to 125 GPa: the anorthite–diopside join. Paper presented at the American Geophysical Union, Fall Meeting 2008 (abstr. #MR32B-04).

Baker D. R. (1992) Tracer diffusion of network formers and multicomponent diffusion in dacitic and rhyolitic melts. *Geochim. Cosmochim. Acta* **56**, 617–631.

Barrat J. L. and Hansen J. P. (2003) *Basic Concepts for Simple and Complex Liquids*. Cambridge University Press.

Bottinga Y. (1985) On the isothermal compressibility of silicate liquids at high pressure. *Earth Planet. Sci. Lett.* **74**, 350–360.

Bouhifd M. A., Jephcoat A. P. and Kelley S. P. (2008) Argon solubility drop in silicate melts at high pressures: a review of recent experiments. *Chem. Geol.* **256**, 252–258.

Brazhkin V. V. and Lyapin A. G. (2003) High-pressure phase transformations in liquids and amorphous solids. *J. Phys. Condens. Mat.* **15**, 6059–6084.

Bryce J. G., Spera F. J. and Stein D. J. (1997) Dependence of self diffusivity on P and T in molten $NaAlSi_2O_6$: comparison of laboratory and molecular dynamics experiments. *Geophys. Res. Lett.* **24**, 711–714.

Bryce J. G., Spera F. J. and Stein D. J. (1999) Pressure dependence of self-diffusion in the $NaAlO_4$–SiO_2 system: compositional effects and mechanisms. *Am. Mineral.* **84**, 345–356.

Canup R. M. (2004) Origin of the terrestrial planets and the Earth–Moon system. *Phys. Today* **57**, 56–62.

Canup R. M. and Agnor C. B. (2000) Accretion of the terrestrial planets and the Earth–Moon system. In *Origin of the Earth and Moon* (eds. R. M. Canup and K. Righter). Univ. of Arizona Press, Tucson, pp. 113–132.

Cao Y., Cormack A., Clare A., Wright A., Sinclair R. and Hannon A. (1994) Points of contact between theory and experiment: a comparison of molecular dynamics and neutron diffraction results. *J. Non-Crystal. Solids* **177**, 317–323.

Car R. and Parrinello M. (1985) Unified approach for molecular dynamics and density-functional theory. *Phys. Rev. Lett.* **55**, 2471–2474.

Chamorro-Perez E., Gillet P., Jambon A., Badro J. and McMillan P. (1998) Low Argon solubility in silicate melts at high pressure. *Nature* **393**, 352–355.

Cohen A. J., Mori-Sanchez P. and Yang W. (2008) Insights into current limitations of density functional theory. *Science* **321**, 792–794.

Darden T., York D. and Pedersen L. (1993) Particle mesh Ewald: an N log (N) method for Ewald sums in large systems. *J. Chem. Phys.* **98**, 10089–10092.

Debaille V., Brandon A. D., Yin Q. Z. and Jacobsen B. (2008) The age, duration, and depth of a turbulent magma ocean in Mars. *Geochim. Cosmochim. Acta* **72**, A205.

Debenedetti P. G. (1996) *Metastable Liquids: Concepts and Principles*. Princeton University Press, Princeton, NJ.

de Koker N. P., Stixrude L. and Karki B. B. (2008) Thermodynamics, structure, dynamics and freezing of Mg_2SiO_4 liquid at high pressure. *Geochim. Cosmochim. Acta* **72**, 1427–1441.

Dove M. T. (1993) *Introduction to Lattice Dynamics*. Cambridge University Press.

Dunn T. (1982) Oxygen diffusion in three silicate melts along the join diopside–anorthite. *Geochim. Cosmochim. Acta* **46**, 2293–2299.

Eyring H., Henderson D., Stover B. J. and Eyring E. M. (1982) *Statistical Mechanics and Dynamics*. John and Wiley and Sons, New York, NY.

Filippini G. and Gavezzotti A. (1993) Empirical intermolecular potentials for organic crystals: the '6-exp' approximation revisited. *Acta Cryst.* **B49**, 868–880.

Frenkel D. and Smit B. (2002) *Understanding Molecular Simulation: From Algorithms to Applications*, second ed. Academic Press, 628 p.

Garnero E. J., Helmberger D. V. and Grand S. (1993) Preliminary evidence for a lower mantle shear wave velocity discontinuity beneath the central Pacific. *Phys. Earth Planet. Inter.* **79**, 335–347.

Garofalini S. H. (2001) Molecular Dynamics Simulations of Silicate Glasses and Glass Surfaces. *Reviews in Mineralogy and Geochemistry* **42**, 131–168.

Ghiorso M. S. (2004a) An equation of state for silicate melts. I. Formulation of a general model. *Am. J. Sci.* **304**, 637–678.

Ghiorso M. S., Nevins D., Cutler I. and Spera F. J. (2009) Molecular dynamics studies of $CaAl_2Si_2O_8$ liquid. II. Equation of state and a thermodynamic model. *Geochim. Cosmochim. Acta.* **73**, 6937–6951.

Ghiorso M. S. (2004b) An equation of state for silicate melts. III. Analysis of stoichiometric liquids at elevated pressure: shock compression data, molecular dynamics simulations and mineral fusion curves. *Am. J. Sci.* **304**, 752–810.

Ghiorso M. S. and Kress V. C. (2004) An equation of state for silicate melts. II. Calibration of volumetric properties at 10^5 Pa. *Am. J. Sci.* **304**, 679–6751.

Ghiorso M. S., Cutler I., Creamer J. B., Nevins D. and Martin G. B. (2008) A thermodynamic theory for dense silicate liquids that includes explicit provision for variation in composition and fluid structure, derived from the Rosenfeld–Tarazona potential energy–temperature scaling law. *Eos Trans. AGU* **89**(53). Fall Meet. Suppl. (abstr. MR43A-1802).

Gray C. G. and Gubbins K. E. (1984) *Theory of molecular fluids*, vol. 1. Fundamentals. Clarendon, 617 p.

Grimsditch M. (1984) Polyamorphism in amorphous SiO_2. *Phys. Rev. Lett.* **52**, 2379–2381.

Guillot B. and Sator N. (2007a) A computer simulation study of natural silicate melts. Part I. Low pressure properties. *Geochim. Cosmochim. Acta* **71**, 1249–1265.

Guillot B. and Sator N. (2007b) A computer simulation study of natural silicate melts. Part II. High pressure properties. *Geochim. Cosmochim. Acta* **71**, 4538–4556.

Haile J. M. (1992) *Molecular Dynamics Simulation: Elementary Methods*. Wiley, New York.

Hanson J. P. and McDonald I. R. (1986) *Theory of Simple Liquids*. Academic Press, New York.

Hinchliffe A. (2000) *Modeling Molecular Structures*. Wiley.

Hohenberg P. and Kohn W. (1964) Inhomogeneous electron gas. *Phys. Rev.* **136**, B864–B871.

Horbach J. and Kob W. (2002) The structural relaxation of molten sodium disilicate. *J. Phys. Condens. Mat.* **14**, 9237–9254.

Jambon A. (1980) Isotopic fractionation: a kinetic model for crystals growing from magmatic melts. *Geochim. Cosmochim. Acta* **44**, 1373–1380.

Karki B., Bhattarai D. and Stixrude L. (2006) First-principles calculations of the structural, dynamical and electronic properties of liquid MgO. *Phys. Rev. B* **73**, 174208.

Kawamura K. (1991) A molecular dynamics simulation of Na_2O–$2SiO_2$–K_2O–$2SiO_2$ melts—effect of basic cell size. *Mol. Simul.* **6**, 245–255.

Kohn W. and Sham L. J. (1965) Self-consistent equations including exchange and correlation effects. *Phys. Rev.* **140**, A1133–A1138.

Kubo R. (1966) The fluctuation–dissipation theorem. *Rep. Prog. Phys.* **29**, 255–284.

Kushiro I. (1981) Viscosity change with pressure of melts in the system CaO–Al_2O_3–SiO_2. *Carnegie I. Wash.* **80**, 339–341.

Lacks D. J., Rear D. B. and Van Orman J. A. (2007) Molecular dynamics investigation of viscosity, chemical diffusivities and partial molar volumes of liquids along the MgO–SiO_2 join as functions of pressure. *Geochim. Cosmochim. Acta* **71**, 1312–1323.

LaTourrette T., Wasserburg G. J. and Fahey A. J. (1996) Self diffusion of Mg, Ca, Ba, Nd, Yb, Ti, Zr, and U in haplobasaltic melt. *Geochim. Cosmochim. Acta* **60**, 1329–1340.

Liang Y., Richter F. M., Davis A. M. and Watson E. B. (1996) Diffusion in silicate melts. I. Self-diffusion in CaO–Al_20_3–SiO_2 at 1500 °C and 1 GPa. *Geochim. Cosmochim. Acta* **60**, 4353–4367.

March N. H. and Tosi M. P. (1984) *Polymers, Liquid Crystals, and Low-dimensional Solids*. Plenum Press, New York.

Martin B., Spera F. J., Ghiorso M. and Nevins D. (2009) Structure, thermodynamic and transport properties of molten Mg_2SiO_4: molecular dynamics simulations and model EOS. *Am. Mineral.* **94**, 693–703.

Matsui M. (1998) Computational modeling of crystals and liquids in the system Na_2O–CaO–MgO–Al_2O_3–SiO_2. In *Properties of Earth and Planetary Materials at High Pressure and Temperature* (eds. M. H. Manghnani and T. Yagi). AGU, Washington, DC, pp. 145–148.

McQuarrie D. A. (1976) *Statistical Mechanics*. Harper Collins, New York.

Mookherjee M., Stixrude L. and Karki B. (2008) Hydrous silicate melt at high pressure. *Nature* **452**, 983–986.

Morgan N. A. and Spera F. J. (2001a) The glass transition, structural relaxation and theories of viscosity: a molecular

dynamics study of amorphous $CaAl_2Si_2O_8$. *Geochim. Cosmochim. Acta* **65**, 4019–4041.

Morgan N. A. and Spera F. J. (2001b) A molecular dynamics study of the glass transition in $CaAl_2Si_2O_8$: thermodynamics and tracer diffusion. *Am. Mineral.* **86**, 915–926.

Mungall J. E., Dingwell D. B. and Chaussidon M. (1999) Chemical diffusivities of 18 trace elements in granitoid melts. *Geochim. Cosmochim. Acta* **63**, 2599–2610.

Nevins D., Spera F. J. and Ghiorso M. S. (2009) Shear viscosity and diffusion in liquid $MgSiO_3$: transport properties and implications for terrestrial planet magma oceans. *Am. Mineral.* **94**, 975–980.

Nevins D. (2009) *Understanding silicate geoliquids at high temperatures and pressures through molecular dynamics simulations*. PhD Dissertation. University of California, Santa Barbara, Santa Barbara.

Nevins D. and Spera F. J. (2007) Accurate computation of shear viscosity from equilibrium molecular dynamics simulations. *Mol. Simul.* **33**, 1261–1266.

Nevins D. and Spera F. (1998) Molecular dynamics simulations of molten $CaAl_2Si_2O_8$: dependence of structure and properties on pressure. *Am. Mineral.* **83**, 1220–1230.

Oganov A. R., Brodholt J. P. and Price G. D. (2001) The elastic constants of $MgSiO_3$ perovskite at pressures and temperatures of the Earth's mantle. *Nature* **411**, 934–937.

Ohtani E., Taulelle F. and Angell C. A. (1985) Al 3 coordination changes in liquid aluminosilicates under pressure. *Nature* **314**, 78–81.

Oishi Y., Terai R. and Ueda H. (1975) Oxygen diffusion in liquid silicates and relation to their viscosity. In *Mass Transport Phenomena in Ceramics* (eds. A. R. Cooper and A. H. Heuer). Plenum Press, New York, pp. 297–310.

Ordejon P., Artacho E. and Soler J. M. (1996) Self-consistent order-*N* density functional calculations for very large systems. *Phys. Rev. B* **53**, 10441–10444.

Philpotts A. R. (1976) Silicate liquid immiscibility; its probable extent and petrogenetic significance. *Am. J. Sci.* **276**, 1147–1152.

Plimpton S. (1995) Fast parallel algorithms for short-range molecular dynamics. *J. Comp. Phys.* **117**, 1–19.

Poe B. T., McMillan P. F., Rubie D. C., Chakraborty S., Yarger J. and Diefenbacher J. (1997) Silicon and oxygen self-diffusivities in silicate liquids measured to 15 Gigapascals and 2800 Kelvin. *Science* **276**, 1245–1248.

Poole P. H., McMillan P. F. and Wolf G. H. (1995) Computer simulations of silicate melts. In *Structure, Dynamics and Properties of Silicate Melts* (eds. J. F. Stebbins, D. B. Dingwell and P. F. McMillan). Mineralogical Society of America, pp. 563–616.

Pohlmann M., Benoit M. and Kob W. (2004) First-principles molecular-dynamics simulations of a hydrous silica melt: structural properties and hydrogen diffusion mechanism. *Phys. Rev. B* **70**, 184209.

Rapaport D. C. (1995) *The Art of Molecular Dynamics Simulation*. Cambridge University Press.

Refson K. (2000) Moldy: a portable molecular dynamics simulation program for serial and parallel computers. *Comp. Phys. Comm.* **126**, 310–329.

Revenaugh J. and Meyer R. (1997) Seismic evidence of partial melt within a possibly ubiquitous low-velocity layer at the base of the mantle. *Science* **277**, 670.

Revenaugh J. and Sipkin S. A. (1994) Seismic evidence for silicate melt atop the 410-km mantle discontinuity. *Nature* **369**, 474–476.

Roedder E. (1951) Low temperature liquid immiscibility in the system K_2O–FeO–Al_2O_3–SiO_2. *Am. Mineral.* **36**, 282–286.

Rosenfeld Y. and Tarazona P. (1998) Density functional theory and the asymptotic high-density expansion of the free energy of classical solids and fluids. *Mol. Phys.* **95**, 141–150.

Rustad J. R., Yuen D. A. and Spera F. J. (1990) Molecular dynamics of liquid SiO_2 under high pressure. *Phys. Rev. A* **42**, 2081–2089.

Rustad J. R., Yuen D. A. and Spera F. J. (1991a) The sensitivity of physical and spectral properties of silica glass to variations of interatomic potentials under high pressure. *Phys. Earth Planet. Inter.* **65**, 210–230.

Rustad J., Spera F. and Yuen D. (1991b) The statistical geometry of amorphous silica at lower mantle pressures – implications for melting slopes of silicates and anharmonicity. *J. Geophys. Res.* **96**, 19665–19673.

Rustad J., Yuen D. and Spera F. J. (1991c) Coordination variability and the structural components of silica glass under high pressures. *Chem. Geol.* **96**, 421–437.

Ryerson F. J. and McKeegan K. D. (1994) Determination of oxygen self-diffusion in akermanite, anorthite, diopside, and spinel: implications for isotopic anomalies and the thermal histories of Ca–Al-rich inclusions. *Geochim. Cosmochim. Acta* **58**, 3713–3734.

Saika-Voivod I., Sciortino F. and Poole P. H. (2001) Computer simulations of liquid silica: equation of state and liquid–liquid phase transition. *Phys. Rev. E* **63**, 011202.

Saika-Voivod I., Sciortino F., Grande T. and Poole P. H. (2004) Phase diagram of silica from computer simulation. *Phys. Rev. E* **70**, 061507.

Scamehorn C. A. and Angell C. A. (1991) Viscosity–temperature relations and structure in fully polymerized aluminosilicate melts from ion dynamics simulations. *Geochim. Cosmochim. Acta* **55**, 721–730.

Senker J. and Rossler E. (2001) Triphenyl phosphite: a candidate for liquid polyamorphism. *Chem. Geol.* **174**, 143–156.

Skibinsky A., Buldyrev S. V., Franzese G., Malescio G. and Stanley H. E. (2004) Liquid–liquid phase transitions for soft-core attractive potentials. *Phys. Rev. E* **69**, 61206.

Soler J. M., Artacho E., Gale J. D., Garcia A. I., Junquera J. and Ordejon P., et al. (2002) The SIESTA method for ab initio order-*N* materials simulation. *J. Phys. Condens. Mat.* **14**, 2745–2780.

Solomatov V. S. (2000) Fluid dynamics of a terrestrial magma ocean. In *Origin of the Earth and Moon* (eds. R. Canup and K. Righter). University of Arizona Press, Tucson, Arizona, pp. 323–338.

Stebbins J. and Poe B. (1999) Pentacoordinate silicon in high-pressure crystalline and glassy phases of calcium disilicate ($CaSi_2O_5$). *Geophys. Res. Lett.* **26**, 2521–2523.

Stebbins J. and Xu Z. (1997) NMR evidence for excess non-bridging oxygen in an aluminosilicate glass. *Nature* **390**, 60–62.

Stein D. J. and Spera F. J. (1995) Molecular dynamics simulations of liquids and glasses in the system $NaAlSiO_4$–SiO_2. I. Methodology and melt structures. *Am. Mineral.* **80**, 417–431.

Stein D. J. and Spera F. J. (1996) Molecular dynamics simulations of liquids and glasses in the system $NaAlSiO_4$–SiO_2: physical properties and transport mechanisms. *Am. Mineral.* **81**, 284–302.

Stixrude L. and Karki B. (2005) Structure and freezing of $MgSiO_3$ liquid in Earth's lower mantle. *Science* **310**, 297–299.

Stone A. J. (2008) Intermolecular potentials. *Science* **321**, 787–789.

Tanaka H. (2000) General view of a liquid–liquid phase transition. *Phys. Rev. E* **62**, 6968–6976.

Tangney P. and Scandolo S. (2002) An *ab initio* parameterized interatomic force field for silica. *J. Chem. Phys.* **117**, 8898–8904.

Taniguchi H. (1992) Entropy dependence of viscosity and the glass-transition temperature of melts in the system diopside–anorthite. *Contrib. Mineral. Petrol.* **109**, 295–303.

Tinker D. and Lesher C. E. (2001) Self-diffusion of Si and O in dacitic liquid at high pressures. *Am. Mineral.* **86**, 1–13.

Tinker D., Lesher C. E., Baxter G. M., Uchida T. and Wang Y. (2004) High-pressure viscometry of polymerized silicate melts and limitations of the Eyring equation. *Am. Mineral.* **89**, 1701–1708.

Valencia D., Sasselov D. D. and O'Connell R. J. (2007) Radius and structure models of the first super-Earth planet. *Astrophys. J.* **656**, 545–551.

Verlet L. (1967) Computer experiments on classical fluids. I. Thermodynamical properties of Lennard–Jones molecules. *Phys. Rev.* **159**, 98–103.

Wan J. T. K., Duffy T. S., Scandolo S. and Car R. (2007) First-principles study of density, viscosity, and diffusion coefficients of liquid $MgSiO_3$ at conditions of the Earth's deep mantle. *J. Geophys. Res.* **112**, B03208. doi:10.1029/2005JB004135.

Watson B. (1982) Basalt contamination by continental crust: some experiments and models. *Contrib. Mineral. Petrol.* **80**, 73–87.

Williams Q. and Garnero E. J. (1996) Seismic evidence for partial melt at the base of Earth's mantle. *Science* **273**, 1528–1530.

Wolf G. H. and McMillan P. F. (1995) Pressure effects on silicate melt structure and properties. *Rev. Mineral. Geochem.* **32**, 505–562.

Ziman J. M. (1972) *Principles of the Theory of Solids*, second ed. Cambridge University Press, Cambridge, 435p.

Associate editor: Kelly Russell